Multidimensional femtosecond correlation spectroscopies of electronic and vibrational excitons

Wei Min Zhang, Vladimir Chernyak, and Shaul Mukamel
Department of Chemistry and Rochester Theory Center for Optical Science and Engineering, University of Rochester, P.O. Box 270216, Rochester, New York 14627

(Received 2 July 1998; accepted 14 December 1998)

Four two-dimensional (2D) four-wave-mixing techniques that can be used to extract information about structure and coupling patterns of interacting chromophores are proposed. These techniques have close conceptual similarities with multiple-pulse NMR spectroscopies. Closed expressions for the signals are derived by solving the nonlinear exciton equations (NEE) which describe the dynamics of multiple excitations using the one-exciton Green function and the exciton–exciton scattering matrix. Possible applications include electronic spectroscopy of aggregates, e.g., photosynthetic antenna complexes, and infrared spectroscopy of localized vibrations (e.g., amid bands in polypeptides). Model calculations are presented for three-chromophore aggregates. © *1999 American Institute of Physics.* [S0021-9606(99)01011-9]

I. INTRODUCTION

Multidimensional coherent spectroscopic techniques are commonly used in multiple-pulse NMR to disentangle complex spectra of many interacting spins by spreading them along several time (or frequency) axes.[1,2] The advent of femtosecond laser pulses[3–8] has made it possible to apply similar concepts in the optical regime.[9–12] In this article we develop a theoretical framework for the design and interpretation of such measurements in systems of localized electronic or vibrational chromophores whose couplings are small compared with their transition frequencies. The model applies to two classes of important systems. First, electronic (visible) excitations in molecular aggregates such as *J* aggregates[13] or the photosynthetic reaction center and LH2 antenna complexes,[14,15] the Fenna–Matthew–Olson (FMO),[16,17] LHC-II complexes,[18,19] and CP29 proteins.[20] Linear spectroscopy yields a few broadened features that depend on numerous factors: such as intermolecular couplings, exciton localization, disorder, and coupling to phonons. It is impossible to pinpoint these various factors unambiguously using the limited information provided by these line shapes. A variety of ultrafast nonlinear spectroscopic techniques, such as pump–probe,[21,22] photon-echo,[23–25] hole-burning[26,27] applied to these aggregates, resulted in an improved understanding of the exciton structure and migration.[28–31] However a systematic methodology for extracting structural information out of these measurements has not been developed yet.

The second type of systems are infrared excitations of coupled localized vibrations. For example, vibrational spectra of the 1600–1700 cm^{-1} amid I band in proteins and polypeptides which originate from the stretching motion of the C═O peptide bond (coupled to in-phase N–H bending and C–H stretching).[32] This mode has a strong transition dipole moment and is clearly distinguishable from other vibrational modes of the amino acid side chains. The localized nature of these modes suggests modeling them as primary excitations whereas the other low-frequency protein and solvent modes can be treated as a thermal bath. The transition dipole moment coupling leads to coherent energy transfer[33] and to the formation of delocalized vibronic excitations (vibrons), analogous to Frenkel excitons.[34] Dependence of the amid I line position on a particular secondary structure is widely utilized in polypeptide and protein structure determination.[35,36] However, a protein usually folds into a complex three-dimensional structure, which consists of several polypeptide segments forming different types of secondary structures.[32] This folding results in strong interactions between remote CO bonds[37] which affects the structure of exciton states and changes the effective dimensionality of the exciton system. Femtosecond IR pump–probe and dynamic hole burning experiments were used recently to investigate the vibrational relaxation and anharmonicity of the amid I vibrations in *N*-methylacetamide (NMA) and three small globular peptides; apamin, scyllatoxin and bovine.[38] Strong coupling to slow vibrational motions leads to exciton localization and self-trapping. Since both effects have a strong dimensionality dependence, the multidimensional spectroscopic signals should carry detailed information on the protein structure.[39,12]

Optical excitations in both types of systems can be separated into manifolds with different numbers of excitons (Fig. 1).[9,34,40] The lowest (single exciton) manifold is accessible using linear optical techniques (e.g., linear absorption) whereas the doubly excited (two-exciton) states can be viewed by third-order spectroscopies.[9] Successively higher manifolds can be probed with higher (e.g., fifth) order techniques. The pattern of multiple excitations provides an extremely sensitive probe for aggregate structure and the connectivity of the various chromophores. Femtosecond techniques can probe the entire manifolds of states in a single measurement. 2D plots can then reveal the correlations between the various chromophore, in complete analogy with multidimensional NMR spectroscopies.[1] Vibrational re-

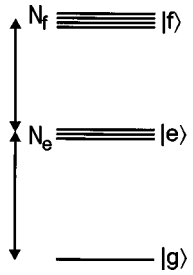

FIG. 1. Energy level diagram of an aggregate made out of N two-level chromophores. $|g\rangle$, the ground state; the number of one-exciton states $|e\rangle$ is $N_e=N$; the number of two-exciton states $|f\rangle$ is $N_f=N(N-1)/2$.

laxation of polyatomic molecules usually proceeds via well defined pathways.[41] Multidimensional measurements could identify these pathways.

Multidimensional spectroscopy of excitons can be analyzed using the nonlinear exciton equations (NEE) (Ref. 42) which provide a collective oscillator picture for exciton dynamics and the nonlinear response. These equations have been gradually developed over the past few years. Spano and Mukamel first showed how theories based on the local field approximation can be extended by adding two-exciton variables to properly account for two-exciton resonances.[43] Other relevant variables have subsequently been identified.[44] In their latest form,[42] the NEE provide a closed Green function expression for the optical response that maintain the complete bookkeeping of time ordering. These expressions will be used in our theoretical modeling. We demonstrate how the 2D response may be measured and analyzed using 2D plots which display the correlations between the various chromophore. In Sec. II, we identify the four possible 2D techniques. Model calculations are presented in Sec. III and our results are finally summarized in Sec. IV. For clarity we have moved all derivations to the Appendices. The Green function expressions for the third-order response function are recasted using the exciton basis in Appendix A. The corresponding frequency domain susceptibility $\chi^{(3)}$ is derived in Appendix B.[45] These results are used in Appendices C and D to calculate the 2D response functions. The final expressions used in our numerical simulation are summarized in Appendix E. A perturbative expression for the signal to first order in interchromophore couplings is given in Appendix F. The expressions for the signals and response functions presented in Appendices A–E avoid the expensive direct calculation of two exciton-states but incorporate their effect through the exciton–exciton scattering matrix.

II. SURVEY AND CLASSIFICATION OF 2D IMPULSIVE TECHNIQUES

We consider a system of N interacting chromophores. The mth chromophore has a primary three-level system denoted S_0, S_1, S_2 with energies 0, Ω_m, and Ω'_m coupled to a bath represented by of a continuous distribution of low frequency modes. The only nonvanishing elements of the dipole operator correspond to the transitions between $S_0\rightarrow S_1$ and $S_1\rightarrow S_2$, and are denoted μ_m and μ'_m, respectively. This model can represent a variety of physical systems such as electronic transitions in molecular aggregates or vibrational transitions in polypeptides. We shall describe this system using an exciton model. To that end, we introduce the exciton-oscillator operators $\hat{B}_n^\dagger$,

$$\hat{B}_n^\dagger \equiv |1\rangle_{n\ n}\langle 0| + \kappa_n |2\rangle_{n\ n}\langle 1|, \tag{2.1}$$

with the commutation relations

$$[\hat{B}_m, \hat{B}_n^\dagger] = \delta_{mn}[1-(2-\kappa_m^2)\hat{B}_m^\dagger \hat{B}_m]. \tag{2.2}$$

The parameter $\kappa_m \equiv \mu'_m/\mu_m$ is the ratio of the two transition dipoles. The polarization operator which describes the coupling to the driving field $\mathcal{E}(t)$ is then given by

$$\hat{P} = \sum_n \mu_n(\hat{B}_n + \hat{B}_n^\dagger). \tag{2.3}$$

As explained in Ref. 42, there is a freedom in constructing the exciton variables $\hat{B}_n$, $\hat{B}_n^\dagger$ through the choice of κ_m. We have used this freedom to make the polarization operator linear in the exciton operators.[42,46,47] This greatly simplifies the final Green function expression for the nonlinear response.

The Hamiltonian which describes the optical response of this model can be represented in the form[42,46]

$$H = \sum_{mn} h_{mn}\hat{B}_m^\dagger \hat{B}_n + \sum_n \frac{g_n}{2}(\hat{B}_n^\dagger)^2(\hat{B}_n)^2 + H_{\rm ph} - \mathcal{E}(t)P, \tag{2.4}$$

where $h_{mn}=\delta_{mn}\hbar\Omega_m + J_{mn}$, with J_{mn} being the hopping matrix and $g_n \equiv 2\hbar(\Omega'_n\kappa_n^{-2}-\Omega_n)$ is an anharmonicity parameter. Both the commutation relations [Eq. (2.2)] and the Hamiltonian contain higher order products of $\hat{B}_n^\dagger$ and $\hat{B}_n$. These higher terms do not contribute to the third order optical response and were neglected. $H_{\rm ph}$ represents the phonon (bath) Hamiltonian which describes vibrational degrees of freedom (intramolecular, intermolecular, and solvent) as well as their coupling to the electronic motions. We shall not specify the phonon Hamiltonian $H_{\rm ph}$, and merely require that it conserves the number of excitons. We treat the bath through relaxation kernels, completely eliminating the vibrational modes. The structure of the final expression for the signals in terms of the relaxation kernels is independent of the specific properties of the bath; the latter only affects the microscopic expressions for the relaxation kernels.[48] The Hamiltonian of Eq. (2.4) establishes the quasiparticle picture of the optical response. Using this Hamiltonian, we view the excitons as oscillator, quasiparticle, degrees of freedom (not merely as states).

A four-wave mixing experiment involves three applied electric fields. The total field $\mathcal{E}(\mathbf{r},t)$ is given by

$$\mathcal{E}(\mathbf{r},t) = \sum_{j=1}^{3} [E_j(t)\exp(i\mathbf{k}_j\mathbf{r} - i\omega_j t) + E_j^*(t)\exp(-i\mathbf{k}_j\mathbf{r} + i\omega_j t)], \tag{2.5}$$

where ω_j, $\mathbf{k}_j$, and E_j is the frequency, wave vector, and envelope of the jth field, respectively. Although the aggregate size is typically small compared to the optical wavelength, the sample is larger than the wavelength, and the

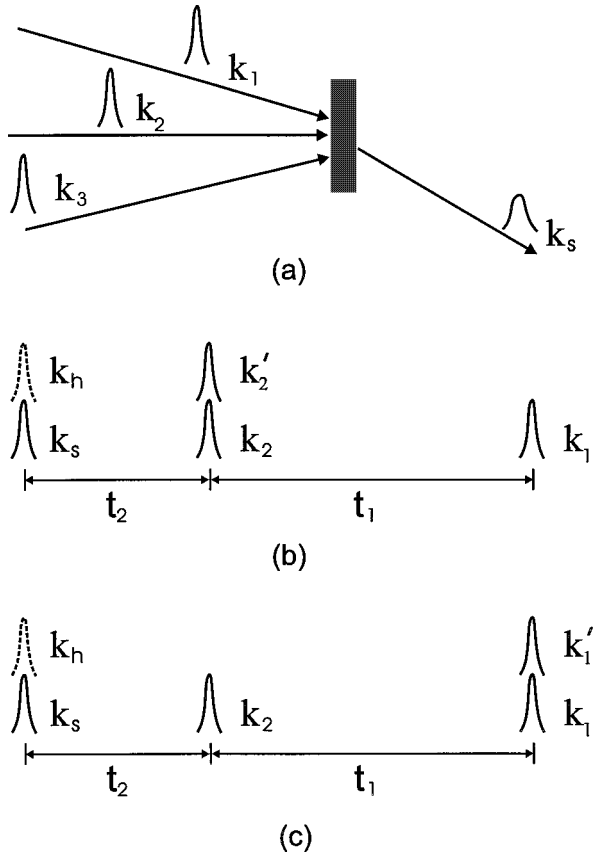

FIG. 2. (a) Pulse configuration for four wave mixing. The signal is generated in all possible directions $\mathbf{k}_s=\pm\mathbf{k}_1\pm\mathbf{k}_2\pm\mathbf{k}_3$. (b) Pulse sequence and time variables for techniques (I) and (IV) where the single pulse comes first followed by the pulse pair. The possible values of $\mathbf{k}_s$ are (I) $\mathbf{k}_s=\mathbf{k}_2'+\mathbf{k}_2-\mathbf{k}_1$, (IV) $\mathbf{k}_s=-\mathbf{k}_2'+\mathbf{k}_2+\mathbf{k}_1$. (c) Pulse sequence and time variables for techniques (II) and (III) where the pulse pair comes first. The possible values of $\mathbf{k}_s$ are (II) $\mathbf{k}_s=-\mathbf{k}_2+\mathbf{k}_1'+\mathbf{k}_1$, (III) $\mathbf{k}_s=\mathbf{k}_2-\mathbf{k}_1'+\mathbf{k}_1$. $\mathbf{k}_h$ is the wave vector of the heterodyne field.

optical signal is subjected to the phase-matching condition.[9,49] This implies that the four-wave mixing signal may only be generated in the directions defined by the wave vectors $\mathbf{k}_s=\pm\mathbf{k}_1\pm\mathbf{k}_2\pm\mathbf{k}_3$.

The heterodyne-detection (time-gated) mode which involves mixing the signal with an additional heterodyne pulse, yields the time resolved signal and also maintains the information about its phase.[3,6,7,50,51] In femtosecond two-dimensional (2D) four-wave mixing spectroscopy, two of the three pulses are time-coincident and only differ by their wave vector. The system thus interacts once with one pulse and twice with a pulse pair. The delay between these two pulses will be denoted t_1. The heterodyne field's delay with respect to the second pulse will be denoted t_2 (see Fig. 2). The heterodyne signal which depends parametrically on these two time intervals is then given by

$$S(t_2,t_1)=\int_{-\infty}^{\infty}d\tau\mathcal{E}_h(\tau)P^{(3)}(\mathbf{r},\tau), \tag{2.6}$$

where $\mathcal{E}_h(\tau)$ is the heterodyne field, and

$$P^{(3)}(\mathbf{r},t)=\int_0^{\infty}dt_3\int_0^{\infty}dt_2\int_0^{\infty}dt_1R(t_3,t_2,t_1)\mathcal{E}(\mathbf{r},t-t_3)\times\mathcal{E}(\mathbf{r},t-t_3-t_2)\mathcal{E}(\mathbf{r},t-t_3-t_2-t_1). \tag{2.7}$$

For our model, the third order nonlinear response function $R(t_3,t_2,t_1)$ can be represented in a form[42]

$$R(t_3,t_2,t_1)=\sum_{j=1}^{3}R_{cj}(t_3,t_2,t_1)+R_i(t_3,t_2,t_1). \tag{2.8}$$

Closed expressions for the coherent contributions R_{cj} for $j=1,2,3$ and the incoherent (sequential) component R_i derived in Ref. 42 are summarized in Appendix A.

Resonant spectroscopy is dominated by contributions which satisfy the rotating wave approximation (RWA). All other terms are highly oscillatory and may be neglected. For the present model, only signals generated in the directions given by $\mathbf{k}_s=\mathbf{k}_1+\mathbf{k}_2-\mathbf{k}_3$ (with all possible permutations of 1, 2, and 3) survive the RWA.[45] We shall distinguish between two pulse configurations. Either the system interacts first with a single pulse ($\mathbf{k}_1$) and then with a pair ($\mathbf{k}_2,\mathbf{k}_2'$) [Fig. 2(b)] or first with a pair ($\mathbf{k}_1,\mathbf{k}_1'$) and then with a single pulse ($\mathbf{k}_2$) [Fig. 2(c)]. Subscripts 1, 2 thus keep track of time ordering (pulse 1 comes first, then 2) whereas wave vectors of time-coincident pulses are distinguished by a prime. By considering all possible signals we have identified the four possible techniques which survive the RWA and differ by the signal's wave vector.[11] (I) The photon echo (PE) technique where $\mathbf{k}_s=\mathbf{k}_2'+\mathbf{k}_2-\mathbf{k}_1$. The impulsive signal is given by $S_I(t_2,t_1)=R_{c1}(t_2,0,t_1)$, where the response function R_{c1} is given by Eq. (A6). (II) The reverse photon echo technique (RPE) $\mathbf{k}_s=-\mathbf{k}_2+\mathbf{k}_1'+\mathbf{k}_1$. This is similar to the photon echo, except that the pulse time ordering is reversed. Here $S_{\mathrm{II}}(t_2,t_1)=R_{c3}(t_2,t_1,0)$ [Eq. (A8)]. (III) The transient grating technique (TG), where $\mathbf{k}_s=\mathbf{k}_2-\mathbf{k}_1'+\mathbf{k}_1$. This is given by $S_{\mathrm{III}}(t_2,t_1)=R_{c1}(t_2,t_1,0)+R_i(t_2,t_1,0)$ [Eqs. (A6) and (A10)]. (IV) The reverse transient grating (RTG) $\mathbf{k}_s=-\mathbf{k}_2'+\mathbf{k}_2+\mathbf{k}_1$. This is similar to the TG except that the pulse time ordering has been reversed and $S_{\mathrm{IV}}(t_2,t_1)=R_{c2}(t_2,0,t_1)$ [Eq. (A7)]. For techniques (I) and (IV) the system interacts twice with the second pulse [Fig. 2(b)] whereas for techniques (II) and (III) a double interaction occurs with the first pulse [Fig. 2(c)]. Each technique is related to specific Liouville space pathways characterizing the evolution of the system's density matrix[9] and therefore tests different ultrafast phenomena, as will be demonstrated in the next section.

At this point we should comment on the relations between the various 2D signals and the four contributions to the response function R_{c1}, R_{c2}, R_{c3}, and R_i. Strictly speaking, optical measurements may not be carried out in the fully impulsive mode since pulse durations are always long compared to the inverse optical frequencies. Instead we consider quasi-impulsive techniques whereby the pulses are short compared to the inverse exciton bandwidth and dephasing times, and their carrier frequencies are resonant with the optical transitions within the pulse spectral width. Under these conditions we may observe electronic and vibrational exciton dephasing in real time. In contrast to the purely impulsive limit, quasi-impulsive signals have additional fast optical-

frequency oscillations. However, as shown in Appendix C, these oscillations can be compensated by varying the relative phases of the pulses with the time delays. The signals are then directly related to the response functions, as indicated above. Since the resonant pulses are long compared with the optical transitions, only the RWA terms survive. Therefore the signals for the four techniques are expressed in terms of specific contributions to R rather than the total response function itself. In Appendix A we present closed expressions for the time-domain response function. In Appendix B we obtain the corresponding expressions for the frequency-domain susceptibility by Fourier transforming the expressions of Appendix A. Expressions for the 2D signals in terms of pulse shapes, time delays and relative phases are derived in Appendix C. Finally in Appendix D we obtain simplified expressions for the signals when the pulses are short compared to the exciton bandwidth and dephasing time. We also choose the relative phases of the pulses to compensate fast oscillations of the signals with the optical frequencies. The signals can then be related directly to specific contributions to the time-domain response function.

A double Fourier transform of the signal $S(t_2,t_1)$ [Eq. (2.6] with respect to t_2 and t_1 yields

$$S_j(\Omega_2,\Omega_1)=\int_0^\infty dt_2\int_0^\infty dt_1\exp(i\Omega_2 t_2+i\Omega_1 t_1)S_j(t_2,t_1). \tag{2.9}$$

This form is particularly useful for displaying structural information, in complete analogy with 2D NMR techniques.[1]

In the following calculations we neglect the sequential contribution R_i (setting $\overline{G}=0$ in Eq. (A10)) and focus on the coherent contributions Eqs. (A6)–(A8). The incoherent term contributes only to the transient grating technique (III) when the time delay (t_1) is comparable with the exciton transport time scale. The following calculations thus apply to techniques I, II, and IV at all times and neglect the long time component of III. This should be the subject of a separate study. We further limit our calculations to impulsive excitations whereby the pulses are short compared with the differences of chromophore frequencies. In this limit the only role of the pulses is the control of the time delays t_1 and t_2 and the precise shapes of the exciting and the heterodyne pulses do not affect the signal (apart from an overall scaling factor). Upon the substitution of Eq. (B8) into Eq. (C9), the impulsive signal adopts the form

$$\begin{aligned}S_j(t_2,t_1)=&|\mathcal{F}|^4\exp[if_j(t_2,t_1)]\frac{1}{(2\pi)^3}\int d\omega_a\int d\omega_b\int d\omega_c\\ &\times\sum_{nm_1m_2m_3}\sum_{n'n''}\mu_n\mu_{m_1}\mu_{m_2}\mu_{m_3}G_{n'm_1}(\omega_a)\\ &\times G_{n'm_2}(\omega_b)G^{\dagger}_{m_3n''}(\omega_c)G_{nn''}(\omega_a+\omega_b-\omega_c)\\ &\times\overline{\Gamma}_{n''n'}(\omega_a+\omega_b)\\ &\times\exp[ig_j(t_2,t_1;\omega_a,\omega_b,\omega_c)],\end{aligned} \tag{2.10}$$

where $j=$I,II,III,IV labels the technique. The single exciton Green function $G(\omega)$ and the exciton–exciton scattering matrix $\overline{\Gamma}(\omega)$ are given in Appendix A. The functions f_j and g_j are defined in Appendix C [Eqs. (C10) and (C11)]. $\mathcal{F}$ denotes the area of the pulse envelope [Eq. (C8)]. Final closed expressions [Eq. (2.9)] for all techniques are given in Appendix E. When the coupling J_{mn} between chromophores is sufficiently weak, it is possible to expand the signal perturbatively in this coupling. The resulting expressions to first order in J_{mn}, which will be helpful in the analysis of these signals, are given in Appendix F.

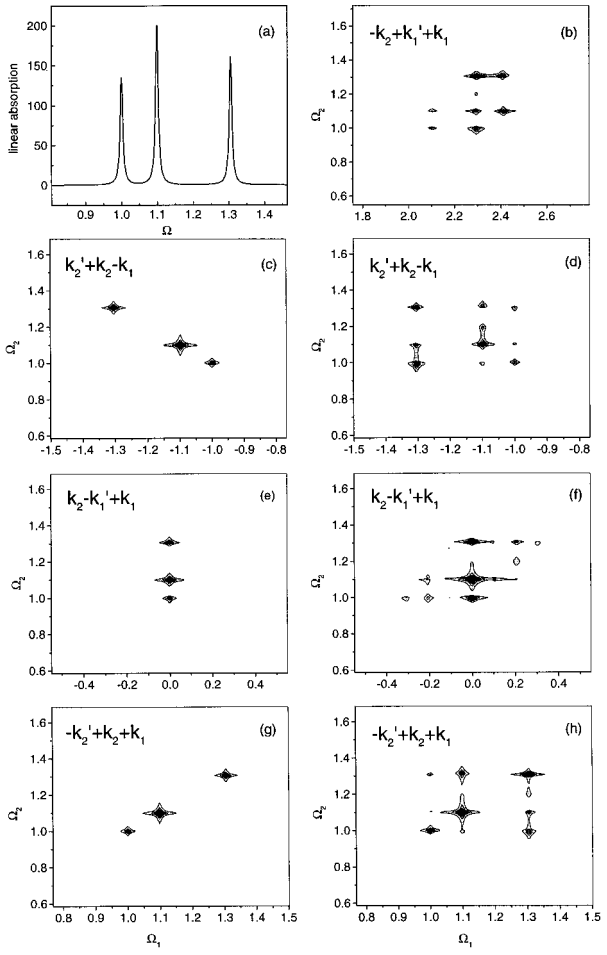

FIG. 3. (Left column) Signals for three uncoupled chromophores A,B,C with $\Omega_A=1$, $\Omega_B=1.1$, $\Omega_C=1.3$ and transition dipole moments $\mu_A=1,\mu_B=1.2,\mu_C=1.1$. (Right column) Signals for three coupled chromophores, $\Omega_A=1.02$, $\Omega_B=1.11$, $\Omega_C=1.28$, $J_{AB}=-0.023$, $J_{BC}=-0.037$, $J_{AC}=0.066$, and $\mu_A=\mu_B=\mu_C=1$. The dephasing rate $\Gamma=0.004$ for both models. These two systems have exactly the same linear absorption (a). Panel (b), reverse echo 2D spectrum. Panels (c) and (d), photon echo; panels (e) and (f), transient grating; panels (g) and (h), reverse transient grating. Comparing the right and left columns shows the signatures of intermolecular couplings.

III. MODEL CALCULATIONS

To demonstrate how multidimensional spectroscopy works, we applied our results to a model three-chromophores system labeled *A*, *B*, and *C*. For simplicity, we assume that each chromophore has only two levels (setting $\kappa_n=0$). This is justified when the third level is well separated from all states of two singly excited chromophores. The corresponding transition frequencies are Ω_A, Ω_B, and Ω_C; transition

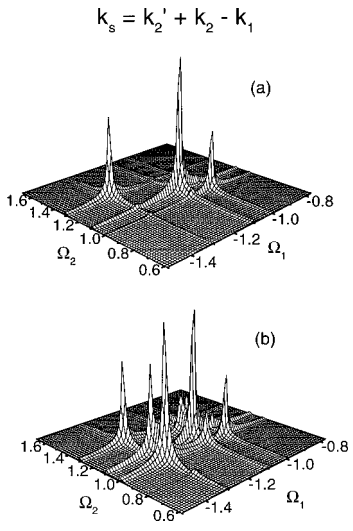

FIG. 4. 3D plot of the resonant four-wave mixing spectra of a 3 chromophore model aggregate. (a) No intermolecular coupling. The signal is diagonal (no cross-peaks). (b) With intermolecular coupling. (a) and (b) corresponds to Figs. 3(c) and 3(d), respectively.

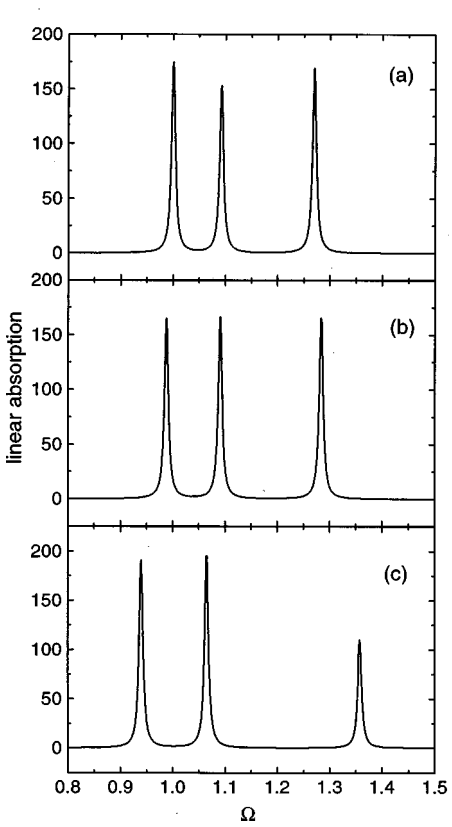

FIG. 5. Linear absorption of three coupled chromophores with $\Omega_A=1$, $\Omega_B=1.09$, $\Omega_C=1.26$, and $\mu_A=\mu_B=\mu_C=1$. Model (a), weak coupling $J_{AB}=-0.014$, $J_{BC}=-0.014$, $J_{AC}=0.029$; model (b), intermediate coupling $J_{AB}=-0.029$, $J_{BC}=-0.029$, $J_{AC}=0.058$; model (c), strong coupling $J_{AB}=-0.086$, $J_{BC}=-0.086$, $J_{AC}=0.115$. The dephasing rate $\Gamma=0.004$ for all three models.

dipole moments μ_A, μ_B, and μ_C; and intermolecular couplings J_{AB}, J_{BC}, and J_{CA}. We further assume a simple exciton dephasing matrix (induced by the phonon bath) where all excitons have the same dephasing rate Γ (see discussion following Eq. (A1)). In all figures we shall give frequencies Ω_j, couplings J and Γ in units of the lowest transition frequency Ω_A. All dipoles are given in units of μ_A.

The linear absorption alone does not reveal the coupling pattern between chromophores. This is illustrated by the following two models. In the first the chromophores are totally decoupled $J_{mn}=0$, $\Omega_A=1$, $\Omega_B=1.1$, $\Omega_C=1.3$ and $\mu_A=1,\mu_B=1.2,\mu_C=1.1$. In the second model, we set $\Omega_A=1.02$, $\Omega_B=1.11$, $\Omega_C=1.28$, $J_{AB}=-0.023$, $J_{BC}=-0.037$, $J_{AC}=0.066$, and $\mu_A=\mu_B=\mu_C=1$. In both models $\Gamma=0.004$. These two models have precisely the same absorption spectrum shown in Fig. 3(a). The 2D spectra are however completely different. In the left column in Fig. 3, we display $|S(\Omega_2,\Omega_1)|$ for the first (no-coupling) model. Only diagonal peaks at the individual chromophore frequencies show up. We introduce the notation (Ω_i,Ω_j) to identify the peaks in the 2D plot. The photon echo shown in panel (c) has diagonal peaks at $(-\Omega_A,\Omega_A)$, $(-\Omega_B,\Omega_B)$, $(-\Omega_C,\Omega_C)$. In panel (e) (transient grating), the peaks are at $(0,\Omega_A)$, $(0,\Omega_B)$, and $(0,\Omega_C)$ whereas for the reverse transient-grating [panel (g)] the peaks are at (Ω_A,Ω_A), (Ω_B,Ω_B), and (Ω_C,Ω_C). Technique II (reverse photon echo) is not shown since the signal vanishes for this model (this will be explained later). In the right column, we display the 2D spectra for the second model where coupling has been added. Panel (b) gives the reverse photon echo. Starting from the second row, we display the 2D spectrum for each technique next to its decoupled model spectrum in the left column. Panel (d) is the photon echo. Apart from the diagonal peaks shown in (c), we observe additional off-diagonal cross peaks, such as $(\Omega_A,\Omega_B)(\Omega_A,\Omega_C)$, etc. Panels (f) and (h) which represent the techniques III (TG) and IV (RTG) show cross peaks as well. A detailed study of these cross peaks will be given in the following figures. At this point suffice it to note that the 2D spectra are capable to distinguish between different coupling patterns even when the linear absorption is identical. This is why 2D spectroscopies constitute such a powerful structural tool. The intensities of the off-diagonal peaks carry information on the magnitudes of intermolecular couplings, while the peak widths represent electronic dephasing. A 3D display of the photon echo spectra shown in Fig. 3 is given in Fig. 4. The first model [Fig. 3(c)] is shown in Fig. 4(a), whereas the second model [Fig. 3(d)] is shown in Fig. 4(b).

We next turn to an in-depth examination of each technique. To that end we introduce the following three models (we use the same dimensionless units introduced in Fig. 3). All models have three chromophores with $\Omega_A=1$, $\Omega_B=1.09$, $\Omega_C=1.26$, $\mu_A=\mu_B=\mu_C=1$, and $\Gamma=0.004$ The models differ by the interchromophore coupling strengths. Model (a) has a weak coupling ($J_{AB}=-0.014$, $J_{BC}=-0.014$, $J_{AC}=0.029$); model (b), intermediate coupling ($J_{AB}=-0.029$, $J_{BC}=-0.029$, $J_{AC}=0.058$); model (c), strong coupling ($J_{AB}=-0.086$, $J_{BC}=-0.086$, $J_{AC}=0.115$). The corresponding linear absorption spectra are displayed in Fig. 5. The relevant states which participate in the third order response are the ground state $|g\rangle$, the manifold of $N_e\equiv N$ one exciton states denoted by $|e\rangle$, and the manifold of $N_f\equiv N(N-1)/2$ two exciton states denoted by $|f\rangle$ (see Fig. 1). For our 3-chromophore aggregate we have $N_e=N_f=3$.

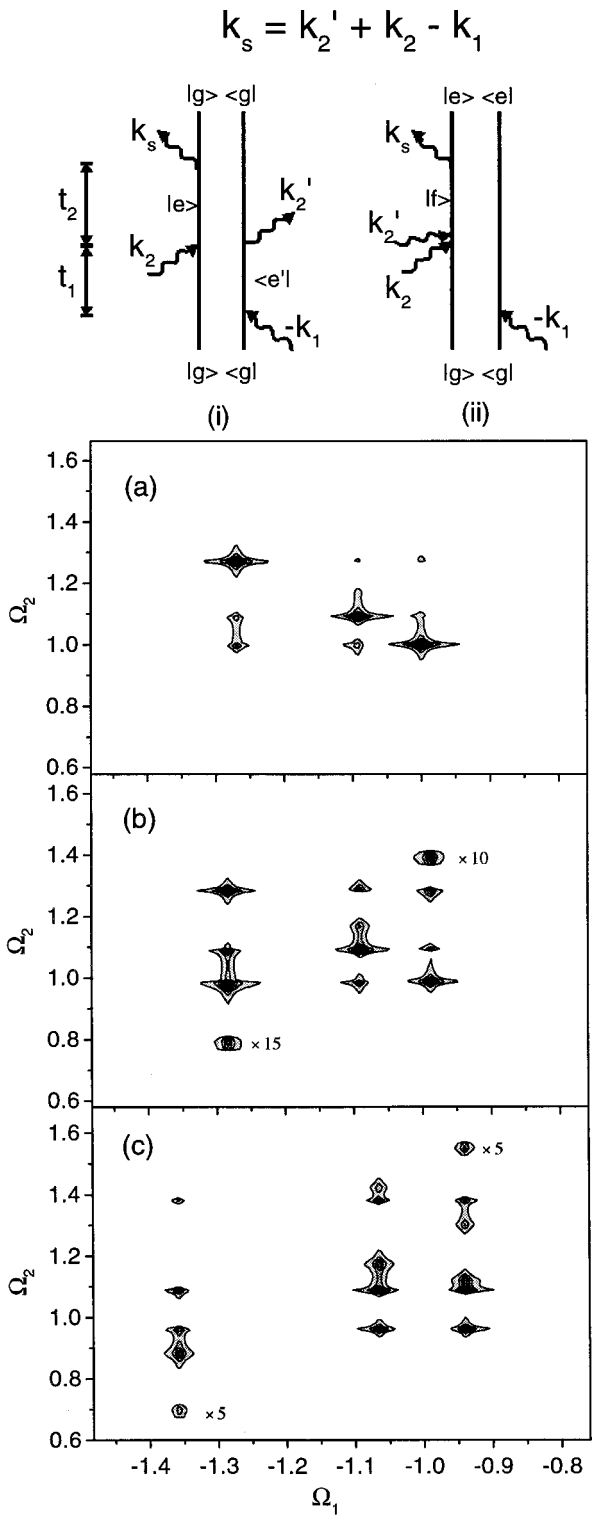

FIG. 6. Photon echo technique for the models used in Fig. 5. (Top) Double-sided Feynman-diagrams. (i) Without two-exciton resonances; (ii) with two-exciton resonances. (a) weak coupling; (b) intermediate coupling; (c) strong coupling.

However for larger aggregates N_f is much larger than N_e.

Figure 6 shows the photon-echo technique. The corresponding double-sided Feynman diagrams are (i) and (ii). The Liouville space pathway represented by (i) only includes one-exciton states while (ii) involves the contribution of two-exciton states as well. During the t_1 period, the system is at the electronic coherence ρ_{ge}. The Fourier transform with respect to t_1 gives N_e peaks at negative frequencies which correspond to the individual excitons. After the double interaction with the second pulse the system is either at $\rho_{e'g}$ (i) or at ρ_{fe} (ii). If the chromophores are uncoupled, the contributions from these two diagrams exactly cancel so that only diagonal peaks appear in the 2D spectrum [Fig. 3(c)]. This is no longer the case once the coupling is switched on. The corresponding resonances can be at all single chromophore frequencies (i) and frequency differences of each one-exciton state to all two-exciton states (ii). The maximum number of Ω_2 peaks for each Ω_1 is N_e+N_f which is six for our model. In practice the number of peaks is considerably smaller for weak coupling since the one exciton energies and the energy differences between one- and two-exciton states are very close, and some peaks may not be resolved. In addition, due to the different coupling patterns, some cross peaks may be too weak to be observed. Equations (F5)–(F7) imply that to first order in intermolecular coupling J, the peaks will appear only at the individual chromophore frequencies, as is clearly shown in Fig. 6(a). By increasing the coupling to intermediate strength (Fig. 6(b)), we observe three additional peaks corresponding to the frequency combinations $(-\Omega_A,\Omega_B+\Omega_C-\Omega_A)$, $(-\Omega_B,\Omega_C+\Omega_A-\Omega_B)$, and $(-\Omega_C,\Omega_A+\Omega_B-\Omega_C)$ which appear in higher orders in J (some peaks are magnified, as indicated, to make them visible). For strong coupling [Fig. 6(c)], we see that several original peaks split into two, reflecting strong exciton effects which result in a frequency shift. All six possible peaks for each Ω_1 are now resolved.

The calculations for Technique II (RPE) are displayed in Fig. 7. The double-sided Feynman diagrams are (iii) and (iv). The system directly goes to the two-exciton manifold after interacting twice with the first pulse and the density matrix is ρ_{fg} during t_1. In the uncoupled case, the signal is represented by the sum of single chromophore contributions. Therefore, it must vanish since our two-level chromophores have no two-exciton states.[52,53] This cancelation makes this technique particularly suitable for structure determination since the entire signal is induced by the coupling. Along the Ω_1 axis, the N_f peaks are located at the two-exciton energies. The possible number of peaks along the Ω_2 axis is $2N_e$, where N_e comes from the transitions between the ground and one exciton states (iii) and the other N_e stands for the energy difference between each two-exciton state and N_e one-exciton states (iv). The corresponding calculations for weak (a), intermediate (b), and strong (c) coupling are displayed. The peaks for weak and intermediate cases can be assigned using single chromophore frequencies. The peaks in Fig. 7(a) are $(\Omega_A+\Omega_B,\Omega_A)$, $(\Omega_A+\Omega_B,\Omega_B)$, $(\Omega_A+\Omega_C,\Omega_A)$, $(\Omega_A+\Omega_C,\Omega_B)$, $(\Omega_A+\Omega_C,\Omega_C)$, $(\Omega_B+\Omega_C,\Omega_B)$, $(\Omega_B+\Omega_C,\Omega_C)$. In contrast to the PE, the strongest off-diagonal peaks now involve linear combinations of chromophore frequencies along Ω_1. This is clearly seen using the perturbative expressions [Eqs. (F8)–(F10)]. Apart from the individual chromophore frequencies along Ω_2, three additional peaks of frequency combinations which appear in higher orders in J show up for intermediate coupling Fig. 7(b). These are $(\Omega_A+\Omega_B,\Omega_A+\Omega_B-\Omega_C)$, $(\Omega_A+\Omega_C,\Omega_A+\Omega_C-\Omega_B)$,

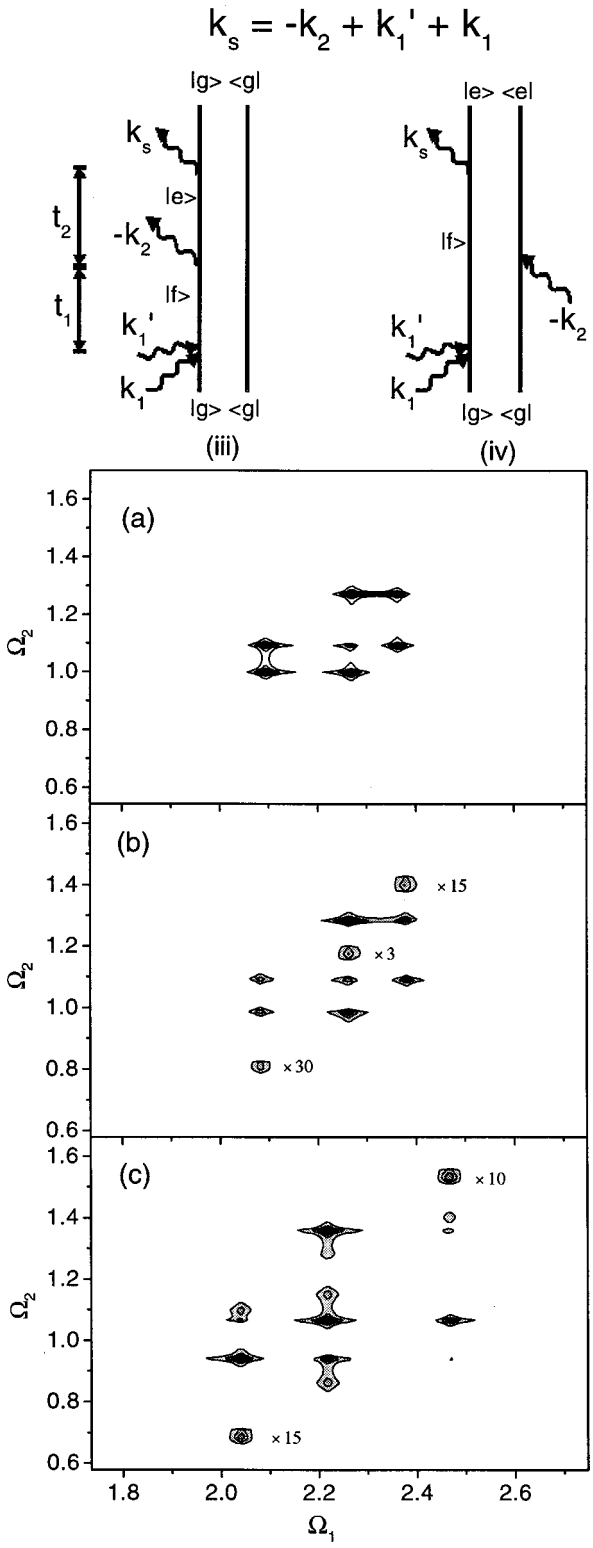

FIG. 7. Reverse photon echo for the models used in Fig. 5. (Top) Double-sided Feynman-diagrams. Both (iii) and (iv) involves two-exciton resonances. (a) Weak coupling; (b) intermediate coupling; (c) strong coupling.

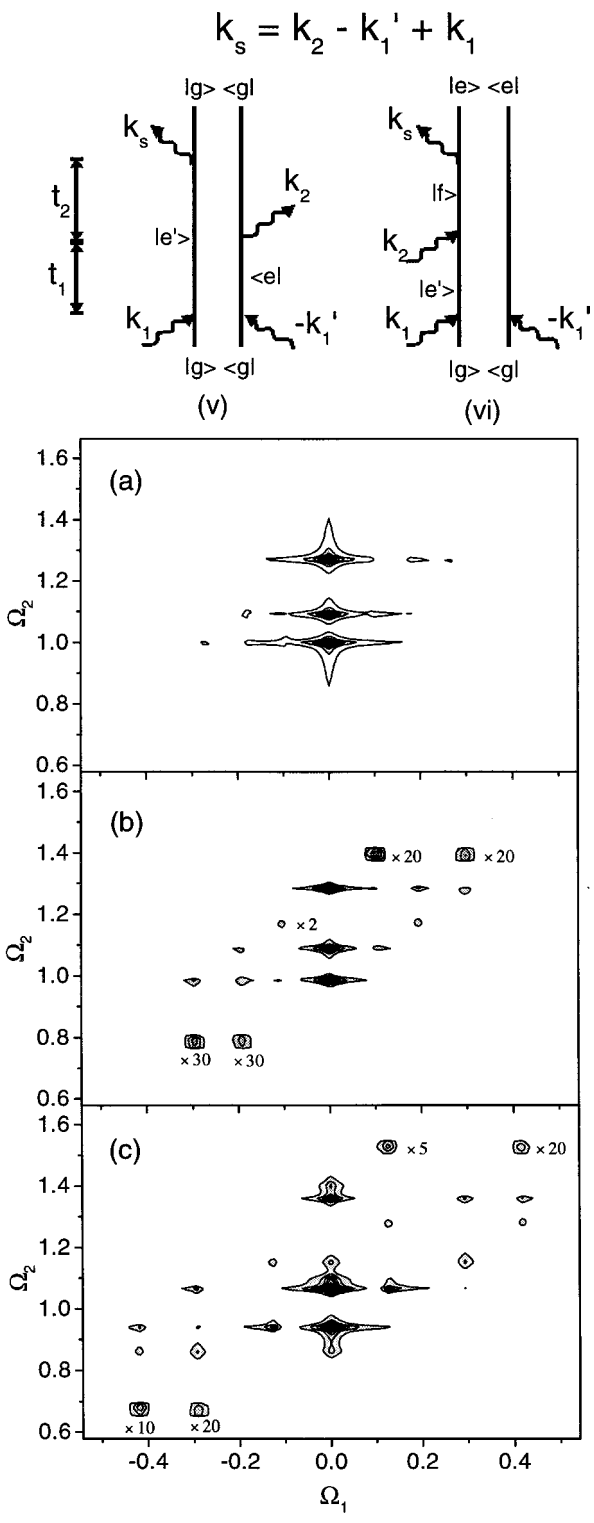

FIG. 8. Transient grating for the models used in Fig. 5. (Top) Double-sided Feynman-diagrams. (v) without two-exciton resonances; (vi) with two-exciton resonances. (a) Weak coupling; (b) intermediate coupling; (c) strong coupling.

$(\Omega_B+\Omega_C, \Omega_B+\Omega_C-\Omega_A)$. Figure 7(c) shows the strong coupling case where all 6 $(2N_e)$ possible peaks are seen.

The third technique (TG) detects the signal in the $\mathbf{k}_2+\mathbf{k}_1'-\mathbf{k}_1$ direction. The double interaction with the first pulse creates populations and interexciton coherences in the excited state, and the relevant Feynman diagrams are (v) and (vi). After the first pulse, the system is in the one-exciton density-matrix $\rho_{e'e}$. The $N_e(N_e-1)+1$ peaks in Ω_1 will appear at energy differences between one-exciton states. If the second pulse brings the $|e\rangle$ state down to the ground state (v), only the Ω_e' frequency will show up during the t_2 period. If the second pulse brings $|e'\rangle$ up to a two-exciton state $|f\rangle$

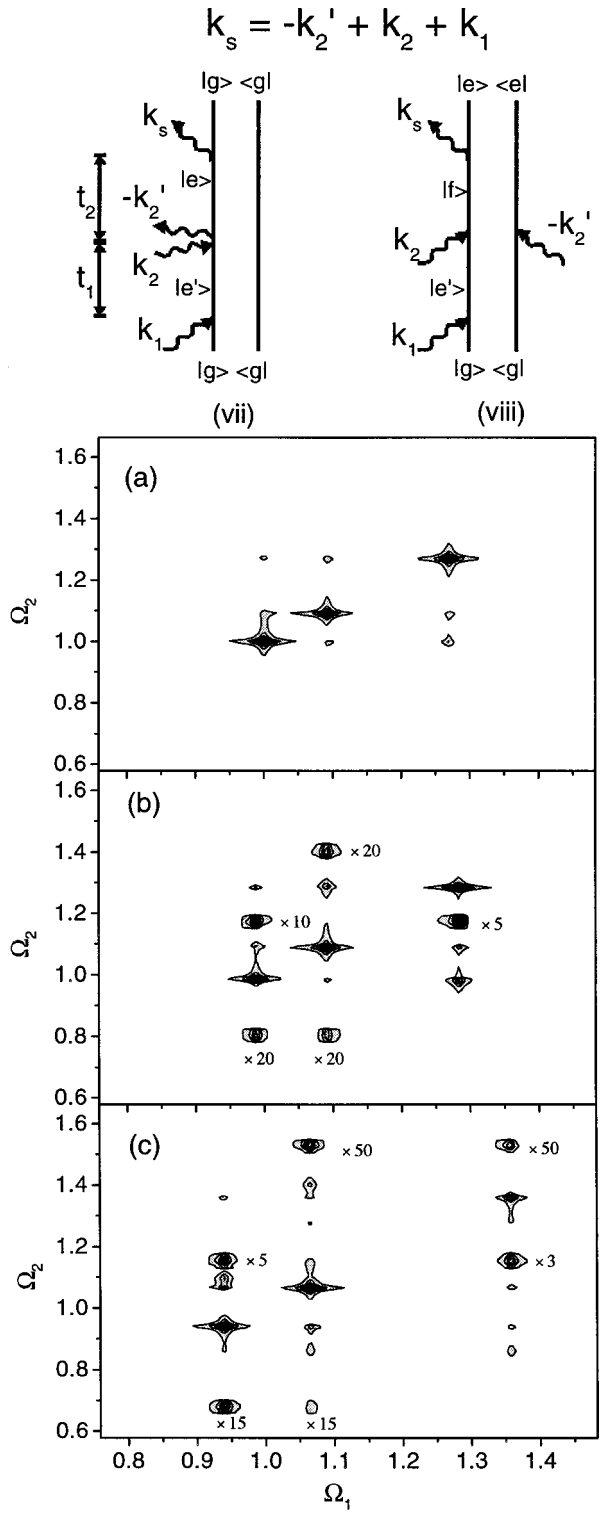

FIG. 9. Reverse transient grating for the models used in Fig. 5. (Top) Double-sided Feynman-diagrams. (vii) Without two-exciton resonances; (viii) with two-exciton resonances. (a) Weak coupling; (b) intermediate coupling; (c) strong coupling.

(vi), all possible frequency differences between $|e\rangle$ and two-exciton states will appear. The maximum number of peaks along the Ω_2 axis is $N_e(1+N_f)$ for $\Omega_1=0$ and $1+N_f$ for $\Omega_1\neq 0$, where 1 comes from the ground to one-exciton state transition (v). For our model, we have maximum 12 peaks for $\Omega_1=0$ and 4 for $\Omega_1\neq 0$. Figures 8(a), 8(b), and 8(c) represent the weak, intermediate, and strong coupling. For the weak coupling Fig. 8(a), only a few cross peaks appear. The main intensity is at the position of the uncoupled chromophores [Fig. 3(e)]. With increasing the coupling Fig. 8(b), additional cross peaks show up at individual chromophore frequencies as well as their combinations, such as $(\Omega_A-\Omega_C,\Omega_A-\Omega_C+\Omega_B)$, $(\Omega_C-\Omega_A,\Omega_C-\Omega_A+\Omega_B)$. With our parameters, we have three one-exciton energies 0.98, 1.08, and 1.28. The peak positions along Ω_1 are at the corresponding differences ± 0.1, ± 0.2, and ± 0.3 [see Fig. 8(b)]. Figure 8(c) represents strong coupling, where peaks split, reflecting strong two-exciton effects.

Figure 9 displays the fourth technique (RTG). The two Feynman diagrams for this technique are (vii) and (viii). During t_1, the system is at $\rho_{e'g}$. Along Ω_1, the N_e peaks appear at positive frequencies. After interacting with the second pulse twice, the density matrix can be either ρ_{eg} (vii) or ρ_{fe} (viii). The maximum number of peaks for each Ω_1 is $N_e+(N_e\cdot N_f)$, which is 12 for $N=3$. Calculations for weak, intermediate, and strong coupling are displayed in Figs. 9(a), 9(b), and 9(c). The spectra for this technique are very similar to the PE (Fig. 6) except that all peaks along Ω_1 now appear at positive frequencies.

Comparing the different techniques, we find that they have some common features. For both the PE and RTG, peaks along Ω_1 only appear at the three individual exciton frequencies. For weak coupling, we have N_e strong diagonal peaks located at $(\pm\Omega_A,\Omega_A)$,$(\pm\Omega_B,\Omega_B)(\pm\Omega_C,\Omega_C)$, and additional cross peaks, described by perturbative expression [Eqs. (F5)–(F7)] and Eqs. [F14)–(F16)]. For intermediate coupling, we obtain additional peaks resulting from interaction of one- and two-exciton states (frequency combinations of individual chromophore). A simple qualitative argument may explain the origin of these combination peaks (compared with the diagonal and cross peaks from the perturbative expression). Since the coupling is not strong, we can still assume that two-exciton states represent approximately two singly excited chromophores. In this case, if we first excite molecule *A* using technique I (PE), we could obtain one additional peak $(-\Omega_A,\Omega_B+\Omega_C-\Omega_A)$ [see Fig. 6(b)], whereas if we use technique IV (RTG), we could obtain two additional peaks $(\Omega_A,\Omega_A\pm(\Omega_B-\Omega_C)$ [Fig. 9(b)]. The second technique (RPE) differs from PE and RTG since the Ω_1 peaks appear at two-exciton energies. We assume that the double interaction with the first pulse excites the two-exciton state $\Omega_A+\Omega_B$. The second pulse gives one extra peak at $(\Omega_A+\Omega_B,\Omega_A+\Omega_B-\Omega_C)$ [Fig. 7(b)]. Transient grating (TG) is very different from the other three techniques, because it creates an exciton population after the interaction with the first pair of pulses. Using the same argument, for $\Omega_1=\Omega_B-\Omega_A$, the combination peak along Ω_2 is at $(\Omega_B-\Omega_A,\Omega_C+\Omega_B-\Omega_A)$, whereas for $\Omega_1=-(\Omega_B-\Omega_A)$, the peak is at $(-(\Omega_B-\Omega_A),\Omega_C-(\Omega_B-\Omega_A))$. This explains why the peaks along Ω_2 for positive Ω_1 appear at higher frequencies compared with negative Ω_1 (see Fig. 8).

With increasing coupling strength, exciton effects start to dominate the signal. This is clearly shown in Figs. 6, 7, 8, and 9. For strong coupling, we observe many additional

peaks reflecting the two exciton interactions. All possible peaks may then be resolved.

When the distances between chromophores are sufficiently large so that the intermolecular coupling constants J_{mn} are smaller than the homogeneous absorption linewidth, the coupling constants which contain the information on the aggregate structure can be determined directly by examining the cross-peak intensities. It is interesting to note that technique II (RPE) shows no diagonal peaks, which reflects the absence of doubly excited states on a single chromophore for the present two-level model. In this case, one can easily obtain J_{mn} from the cross peak intensities. For strong intermolecular coupling (J is of the order of the differences between the chromophore transition frequencies) excitonic effects become dominant. The perturbative expansion in J no longer holds and the peak positions are shifted. The information on the magnitude of J is now contained in both the peak positions and intensities, and is not as easy to extract as in the weak coupling limit.

IV. DISCUSSION

In this paper we have proposed new two-dimensional femtosecond resonant spectroscopic techniques which have the capacity to probe directly the excitonic couplings among chromophores. Our calculations illustrate how 2D techniques, unlike conventional 1D measurements, provide information on intermolecular coupling constants, which could fully characterize the system. By inverting the signals it should become possible to extract detailed structural information, in complete analogy with 2D NMR spectroscopies. These techniques should be most valuable for electronic excitations of aggregates as well as for infrared studies of vibrational excitons.[37,38]

Our calculations are based on a closed form expression for the third-order nonlinear response derived by solving the nonlinear exciton equations (NEE). This procedure avoids the expensive explicit calculation of two exciton states (which is the bottleneck in such calculations) and instead incorporates their effects through a scattering matrix. We identified four heterodyne techniques that differ by the pulse sequence and the direction of observation, and systematically varied the coupling strengths and patterns. The interpretation of the signals is particularly simple when $J \ll \Gamma$, Γ being the electronic homogeneous dephasing rate, since in this approach the strong cancelations of terms which complicate the more conventional sum-over-states (SOS) expressions[9] are automatically built in. Expansion of Eq. (F4) in powers of J shows that for $J=0$ the signal $S(\Omega_2,\Omega_1)$ is given by the sum of contributions from individual chromophores and, therefore, is represented by a set of diagonal peaks located at $\Omega_2 = \pm \Omega_1$; peak positions reflect the chromophore transition frequencies whereas their widths represent the magnitude of Γ. To first-order in J, the signal is represented by a series of new off-diagonal peaks. The Ω_2, Ω_1 coordinates of a peak centers correspond to the transition frequencies of different chromophores. The intensities of these off-diagonal peaks reflect the intermolecular coupling constants. To second order in J, new cross peaks whose positions involve linear combinations of the chromophore frequencies appear as well.

The present study could be extended in various directions. Our calculations used a model trimer aggregate with relatively large transition frequency differences between chromophores (2000–4000 cm^{-1} for transition frequencies in the visible range). This corresponds to aggregates formed by chemically different chromophores. Our calculations clearly illustrate the capacity of femtosecond optical techniques to study such aggregates. Many interesting systems are however made out of chemically identical chromophores. Examples are molecular dimers and trimers, e.g., arrays of covalently linked porphyrins[54,55] which mimic the architectural properties of light harvesting systems as well as the B850 band of the LH2 complex of purple bacteria. In these systems, differences between the chromophore transition frequencies due to structural heterogenity is typically several hundred wave numbers, which is comparable with the homogeneous dephasing rates. Resolving the various peaks then becomes a more difficult task. Recent calculations[11] showed how a combination of femtosecond 2D techniques may be used to determine all parameters of a homogeneous molecular dimer; the coupling constant and the homogeneous and inhomogeneous broadening. Higher dimensional (3D, 4D, etc.) time-domain techniques should be developed and applied to study larger homogeneous aggregates with more than two chromophores.

The expression for the 2D response [Eqs. (A6)–(A8) and Eq. (A10)] as well as $\chi^{(3)}$ [Eq. (B7)] incorporate the effects of exciton transport. Our numerical studies however focused on the coherent terms alone. The incoherent (sequential) contribution Eq. (A10) which carries useful information about exciton relaxation has been neglected. The study of techniques specifically designed to probe transport is an important problem for future studies. A transient grating study of exciton transport which incorporates the incoherent contribution to the response should be of considerable interest. A systematic procedure for extracting the intermolecular couplings out of the multidimensional spectroscopic data needs to be developed. For example, the exciton coupling may often be given by the dipole–dipole interaction tensor which has a well defined dependence on relative orientation and distances of the interacting dipoles. It should then be possible to invert the 2D spectrum to obtain the three-dimensional conformation.

Our calculations were restricted to two-level chromophores and the role of additional levels remains to be studied. In our three chromophore model $N_e = N_f = 3$. For larger aggregates $N_f \gg N_e$ and the two exciton manifold will become much richer. Additional information may be obtained by other extensions. For example, one can vary the pulse shapes and phases $\varphi(t_2,t_1)$ and scan them in addition to the pulse delays. More detailed mechanisms of homogeneous dephasing and inhomogeneous broadening need to be incorporated. Line broadening and finite pulse durations may complicate the analysis and may wash out some of the information. However, in analogy with NMR, it should be possible to design new types of pulse sequences specifically taylored towards overcoming these difficulties.

ACKNOWLEDGMENTS

S.M. wishes to thank the Guggenheim Fellowship and the Alexander von Humboldt Fellowship. The hospitality of Professor E. Schlag is greatly appreciated. The support of the Air Force office of scientific research through Grant No. AFOSR-95-F49620-96-1-0030, the National Science Foundation through Grant No. CHE-9526125 and NSF Rochester Theory Center for Optical Science and Engineering through Grant No. PHY94-15583 is gratefully acknowledged.

APPENDIX A: THIRD ORDER RESPONSE FUNCTION IN THE EXCITON REPRESENTATION

The nonlinear response function $R(t_3,t_2,t_1)$ in Eq. (2.7) can be obtained by solving the nonlinear exciton equations of motions (NEE) [Eqs. (2.25)–(2.28) of Ref. 42]. The resulting Green function expressions (GFE) for the nonlinear response function [Eqs. (3.14)–(3.18) of Ref. 42] can be recast in the form of Eq. (2.8). The response function derived in Ref. 42 has five terms. The first three do not involve the incoherent exciton density matrix relaxation and are therefore referred to as the coherent contributions. They are expressed in terms of the one-exciton Green function $G_{mn}(\tau)$ and the two-exciton scattering matrix $\bar{\Gamma}_{mn}(\omega)$. Eliminating the bath degrees of freedom yields the one-exciton green function[42,45]

$$G_{nn'}(t)=\theta(t)[\exp(-i\hat{h}t-\hat{\Gamma}t)]_{nn'}, \tag{A1}$$

where $\hat{h}$ is the operator with matrix elements h_{mn} [Eq. (2.4)] and $\hat{\Gamma}$ is the phonon-induced one-exciton dephasing operator with matrix elements Γ_{mn}. Our primary interest in this article is concerned with extracting structural information. We shall therefore use the simplest model for dephasing and assume the following form for the dephasing matrix $\Gamma_{mn}=\Gamma\delta_{mn}$. The optical response is obtained from that for a system without a bath by adding phonomenological damping with the rate Γ. This considerably simplifies the final expressions for the signals, yet retains all qualitative features of the ultrafast coupled system-bath dynamics.[56] The one-exciton Green function is then given by

$$G_{nn'}(t)=\theta(t)\sum_{\alpha}\psi_{\alpha}(n)\psi^{*}_{\alpha}(n')\exp(-i\epsilon_{\alpha}t-\Gamma t), \tag{A2}$$

where $\psi_{\alpha}(n)$ are the eigenvectors of the one-exciton Hamiltonian h_{mn} with the eigenvalues ϵ_{α}. The two-exciton Green function is calculated through the $N\times N$ scattering matrix $\tilde{\Gamma}$ (Refs. 42,46,57), which has the following form in the frequency domain:

$$\bar{\Gamma}_{mn}(\omega)=[F(\omega)]^{-1}_{mn}[(\hbar\omega+g_n)\kappa_n^2-2\hbar\omega], \tag{A3}$$

with

$$F(\omega)=\delta_{mn}\kappa_m^2-[(\hbar\omega+g_n)\kappa_n^2-2\hbar\omega]\mathcal{G}_{mn}(\omega), \tag{A4}$$

and the zero-order two-exciton Green function is given by

$$\mathcal{G}_{mn}(\omega)\equiv\int_{-\infty}^{\infty}\frac{d\omega'}{2\pi i}G_{mn}(\omega')G_{mn}(\omega-\omega'). \tag{A5}$$

Upon the substitution of Eq. (A2) in Eqs. (4.14)–(4.18) of Ref. 42 and carrying out the integral of τ' and τ'', we recast these terms in the exciton basis set

$$\begin{aligned}R_{c1}(t_3,t_2,t_1)&=i^3\sum_{\alpha_1\alpha_2\alpha_3\alpha_4}\mu_{\alpha_4}\mu_{\alpha_3}\mu^{*}_{\alpha_2}\mu^{*}_{\alpha_1}\frac{1}{2\pi}\int_{-\infty}^{\infty}d\omega'\\&\quad\bar{\Gamma}_{\alpha_4\alpha_3,\alpha_1\alpha_2}(\omega')\exp(i\epsilon_{\alpha_3}t_1-\Gamma t_1)\\&\quad\times\exp[-i(\epsilon_{\alpha_1}-\epsilon_{\alpha_3})t_2-2\Gamma t_2]\\&\quad\times\frac{\exp[-i(\omega'-\epsilon_{\alpha_3})t_3-\Gamma t_3]}{(\omega'-\epsilon_{\alpha_1}-\epsilon_{\alpha_2}+2i\Gamma)(\omega'-\epsilon_{\alpha_3}-\epsilon_{\alpha_4}+i\gamma_0)},\end{aligned} \tag{A6}$$

$$\begin{aligned}R_{c2}(t_3,t_2,t_1)&=i^3\sum_{\alpha_1\alpha_2\alpha_3\alpha_4}\mu_{\alpha_4}\mu_{\alpha_3}\mu^{*}_{\alpha_2}\mu^{*}_{\alpha_1}\frac{1}{2\pi}\int_{-\infty}^{\infty}d\omega'\\&\quad\bar{\Gamma}_{\alpha_4\alpha_3,\alpha_1\alpha_2}(\omega')\exp(-i\epsilon_{\alpha_2}t_1-\Gamma t_1)\\&\quad\times\exp[-i(\epsilon_{\alpha_2}-\epsilon_{\alpha_3})t_2-2\Gamma t_2]\\&\quad\times\frac{\exp[-i(\omega'-\epsilon_{\alpha_3})t_3-\Gamma t_3]}{(\omega'-\epsilon_{\alpha_1}-\epsilon_{\alpha_2}+2i\Gamma)(\omega'-\epsilon_{\alpha_3}-\epsilon_{\alpha_4}+i\gamma_0)},\end{aligned} \tag{A7}$$

$$\begin{aligned}R_{c3}(t_3,t_2,t_1)&=i^3\sum_{\alpha_1\alpha_2\alpha_3\alpha_4}\mu_{\alpha_4}\mu_{\alpha_3}\mu^{*}_{\alpha_2}\mu^{*}_{\alpha_1}\frac{1}{2\pi}\int_{-\infty}^{\infty}d\omega'\\&\quad\bar{\Gamma}_{\alpha_4\alpha_3,\alpha_1\alpha_2}(\omega')\exp(-i\epsilon_{\alpha_1}t_1-\Gamma t_1)\exp(-i\omega' t_2)\\&\quad\times\frac{\exp[-i(\omega'-\epsilon_{\alpha_3})t_3-\Gamma t_3]-\exp(-i\epsilon_{\alpha_4}t_3-\Gamma t_3)}{(\omega'-\epsilon_{\alpha_1}-\epsilon_{\alpha_2}+2i\Gamma)(\omega'-\epsilon_{\alpha_3}-\epsilon_{\alpha_4}+i\gamma_0)}.\end{aligned} \tag{A8}$$

Here

$$\bar{\Gamma}_{\alpha_4\alpha_3,\alpha_1\alpha_2}(\omega)=\sum_{mn}\psi^{*}_{\alpha_4}(m)\psi^{*}_{\alpha_3}(m)\bar{\Gamma}_{mn}(\omega)\psi_{\alpha_1}(n)\psi_{\alpha_2}(n) \tag{A9}$$

represents the exciton scattering matrix in the exciton basis set. γ_0 should be smaller than the imaginary parts of all poles of the two-exciton Green function (i.e., $\sim 2\Gamma$, see Appendix B). The expressions for the coherent part of R [Eqs. (A6)–(A8)] can be alternatively derived using simplified NEE equations for one- and two-exciton variables derived in Ref. 46 and adding the dephasing to the one-exciton Green functions G_{mn} phenomenologically. These equations neglect the effects of exciton transport and, therefore, reproduce the coherent contributions only.

The two remaining (incoherent) contributions are given by Eqs. (3.17)–(3.18) of Ref. 42 which do involve the exciton transport and can be combined into a single term in the exciton basis

$$R_i(t_3,t_2,t_1)$$
$$=-4\sum_{\alpha_1\alpha_2\alpha_3\alpha_4\alpha_5\alpha_6}\mu_{\alpha_4}\mu_{\alpha_5}\mu^*_{\alpha_1}\mu^*_{\alpha_2}\frac{1}{(2\pi)^2}\int_{-\infty}^{\infty}d\omega'$$
$$\int_{-\infty}^{\infty}d\omega''\overline{\Gamma}_{\alpha_3\alpha_4,\alpha_6\alpha_2}(\omega')\overline{G}_{\alpha_6\alpha_3,\alpha_1\alpha_5}(\omega'')$$
$$\times\cos(\epsilon_{\alpha_1}t_1)\exp(-\Gamma t_1)$$
$$\times\frac{\exp(-i\omega''t_2)\exp[-i(\omega'-\epsilon_{\alpha_3})t_3-\Gamma t_3]}{(\omega'-\epsilon_{\alpha_3}-\epsilon_{\alpha_4}+i\gamma_0)(\omega'-\omega''-\epsilon_{\alpha_2}-\epsilon_{\alpha_3}+i\gamma_0)}. \tag{A10}$$

This term depends on the Redfield tensor $\overline{R}^{mn}_{ij}$ related to the relaxation of the one-exciton density matrix $\langle\hat{B}^\dagger_n\hat{B}_m\rangle$ (incoherent exciton motion). The latter is described by the irreducible part $\overline{G}_{mn,kl}(t)$ of the Green function for the Redfield equation,[58,59]

$$\overline{G}_{\alpha_6\alpha_3,\alpha_1\alpha_5}(\omega)=\sum_{mn}\psi^*_{\alpha_6}(m)\psi^*_{\alpha_3}(m')$$
$$\times\overline{G}_{mm',nn'}(\omega)\psi_{\alpha_1}(n)\psi_{\alpha_5}(n'), \tag{A11}$$

is the exciton representation of the Green function $\overline{G}_{mm',nn'}(\omega)$.

APPENDIX B: THE THIRD ORDER SUSCEPTIBILITY

The third-order optical susceptibility $\chi^{(3)}(-\omega_s;\omega_a,\omega_b,\omega_c)$ can be derived by Fourier transforming the expressions for the time domain response functions given in Appendix A. The Fourier transform is conveniently carried out with respect to the actual interaction times with the driving field which are denoted (in chronological orders) τ_1, τ_2, and τ_3. They are connected to the time-interval varibles of Appendix A by $t_1=\tau_2-\tau_1$, $t_2=\tau_3-\tau_2$, $t_3=t-\tau_3$,

$$P^{(3)}(\mathbf{r},t)=\int_0^t d\tau_3\int_0^{\tau_3}d\tau_2\int_0^{\tau_2}d\tau_1 R(t,\tau_3,\tau_2,\tau_1)$$
$$\times\mathcal{E}(\mathbf{r},\tau_3)\mathcal{E}(\mathbf{r},\tau_2)\mathcal{E}(\mathbf{r},\tau_1), \tag{B1}$$
$$R(t,\tau_3,\tau_2,\tau_1)=R_c(t,\tau_3,\tau_2,\tau_1)+R_i(t,\tau_3,\tau_2,\tau_1). \tag{B2}$$

We start with the coherent contribution [Eqs. (3.14)–(3.16) of Ref. 42]. Switching to the actual time representation they can be combined which yields the coherent part of the response function

$$R_c(t;\tau_3,\tau_2,\tau_1)$$
$$=(-i^3)\sum_{perm}\sum\mu_n\mu_{m_1}\mu_{m_2}\mu_{m_3}\int_{-\infty}^{\infty}d\tau''\int_{-\infty}^{\infty}d\tau'$$
$$\times G_{n'm_1}(\tau'-\tau_1)G_{m'm_2}(\tau'-\tau_2)G^\dagger_{m_3m''}(\tau''-\tau_3)$$
$$\times G_{nn''}(t-\tau'')\overline{\Gamma}_{n''m'',n'm'}(\tau''-\tau')+\text{c.c.}, \tag{B3}$$

where Σ_{perm} denotes the summation over the permutations of the times τ_1, τ_2, and τ_3. The integrations over τ' and τ'' in Eq. (B3) run from $-\infty$ to ∞ since the Green functions $G(\tau)$ and the scattering matrix $\overline{\Gamma}(\tau)$ are nonzero for $\tau>0$ only. The two incoherent contributions [Eqs. (3.17) and (3.18) of Ref. 42] can be represented in a form

$$R_i(t;\tau_3,\tau_2,\tau_1)=2\sum_{perm}\sum\mu_n\mu_{m_1}\mu_{m_2}\mu_{m_3}\int_{-\infty}^{\infty}d\tau'''\int_{-\infty}^{\infty}d\tau''\int_{-\infty}^{\infty}d\tau' G_{nn''}(t-\tau'')G_{n'm_3}(\tau'-\tau_3)G^\dagger_{im''}(\tau''-\tau')$$
$$\times\overline{\Gamma}_{n''m'',n'm'}(\tau''-\tau')\overline{G}_{m'i,kj}(\tau'-\tau''')[G_{km_1}(\tau'''-\tau_1)\delta_{m_2j}\delta(\tau'''-\tau_2)+G^\dagger_{m_2j}(\tau'''-\tau_2)\delta_{m_1k}\delta(\tau'''-\tau_1)]+\text{c.c.} \tag{B4}$$

Equations (B3) and (B4) are written in the molecular basis set as opposed to Eqs. (A6)–(A11) which use the exciton basis set. The Fourier transform is carried out by expressing $G(\tau)$, $\overline{G}(\tau)$, and $\overline{\Gamma}(\tau)$ in Eqs. (B3) and (B4) in terms of their Fourier transforms $G(\omega)$, $\overline{G}(\omega)$, and $\overline{\Gamma}(\omega)$. Integrations over times can be then performed explicitly which yields delta functions of combinations of frequencies. Retaining only those terms which survive the rotating wave approximation we finally obtain the nonlinear susceptibility.[9,60] In four-wave mixing spectroscopy, $P(\mathbf{r},t)$ can be represented using the third-order optical susceptibility $\chi^{(3)}(-\omega_s;\omega_a,\omega_b,\omega_c)$,

$$P(\mathbf{r},t)=\frac{1}{(2\pi)^3}\int d\omega_a\int d\omega_b\int d\omega_c\exp(-i\omega_s t)$$
$$\times\chi^{(3)}(-\omega_s;\omega_a,\omega_b,\omega_c)\overline{\mathcal{E}}(\mathbf{r},\omega_a)$$
$$\times\overline{\mathcal{E}}(\mathbf{r},\omega_b)\overline{\mathcal{E}}(\mathbf{r},\omega_c), \tag{B5}$$

where

$$\overline{\mathcal{E}}(\mathbf{r},\omega)\equiv\int_{-\infty}^{\infty}\mathcal{E}(\mathbf{r},t)\exp(i\omega t)dt, \tag{B6}$$

is the driving field in the frequency domain and $\mathbf{r}$ denotes the position of an aggregate whose size is smaller than the opti-

cal wavelength (Latin indices ω_a, etc. denote fields with no particular time-ordering). Equation (B5) is obtained by first expressing the Fourier transform $P(\omega)$ of the polarization in terms of $\bar{\mathcal{E}}(\omega)$ using the $\chi^{(3)}$ and then returning to the time domain,

$$\chi^{(3)}(-\omega_s;\omega_a,\omega_b,\omega_c) = \chi_c^{(3)}(-\omega_s;\omega_a,\omega_b,\omega_c)+\chi_i^{(3)}(-\omega_s;\omega_a,\omega_b,\omega_c), \tag{B7}$$

where $\omega_s=\omega_a+\omega_b+\omega_c$. The coherent contribution $\chi_c^{(3)}$ is given by[9,61]

$$\chi_c^{(3)}(-\omega_s;\omega_a,\omega_b,\omega_c) = \frac{1}{3!}\sum_{p(\omega_a,\omega_b,\omega_c)}\sum_{nm_1m_2m_3}\sum_{n'n''}\mu_n\mu_{m_1}\mu_{m_2}\mu_{m_3} \times G_{n'm_1}(\omega_a)G_{n'm_2}(\omega_b)G^{\dagger}_{m_3n''}(-\omega_c) \times G_{nn''}(\omega_s)\bar{\Gamma}_{n''n'}(\omega_a+\omega_b)+\text{c.c.}, \tag{B8}$$

and the summation $p(\omega_a,\omega_b,\omega_c)$ is over all $3!=6$ permutations of frequencies ω_a, ω_b, and ω_c.

The incoherent contribution $\chi_i^{(3)}$ adopts the form

$$\chi_i^{(3)}(-\omega_s;\omega_a,\omega_b,\omega_c) = \frac{1}{3!}\sum_{p(\omega_a,\omega_b,\omega_c)}\sum\mu_n\mu_{m_1}\mu_{m_2}\mu_{m_3}\int_{-\infty}^{\infty}\frac{d\epsilon}{2\pi}G_{nn''}(\omega_s) \times G_{n'm_3}(\omega_b)G^{\dagger}_{im''}(\epsilon)\bar{\Gamma}_{n''m'',n'm'}(\omega_a+\omega_b+\omega_c-\epsilon) \times\bar{G}_{m'i,kj}(\omega_a+\omega_c)[G_{km_1}(\omega_a)\delta_{m_2j} + G^{\dagger}_{m_2j}(-\omega_c)\delta_{km_1}]+\text{c.c.}. \tag{B9}$$

Equations (B7)–(B9) can be alternatively derived by using a diagrammatic perturbative expansion in the exciton–phonon coupling followed by a resummation of the leading contributions.[45]

In the RWA only those contributions in Eqs. (B8) and (B9) survive for which the one-exciton are taken at positive frequencies which implies $\omega_a,\omega_b>0$, $\omega_c<0$. In particular this implies that in the RWA only the permutations of ω_a and ω_b are allowed.

APPENDIX C: THE 2D TIME-DOMAIN RESPONSE

In this Appendix we derive closed expressions for the 2D signals starting with the third-order optical susceptibility $\chi^{(3)}$. The time-domain heterodyne detected signal is proportional to the polarization $P(t)$, which is given by Eq. (2.7).

Introducing the carrier frequency of the pulses $\bar{\omega}_1$, $\bar{\omega}_2$, $\bar{\omega}_3$ the envelopes $E_1(\tau)$, $E_2(\tau)$, $E'(\tau)$ and assuming that the pulses come at times $\tau=-t_1-t_2$ and $\tau=-t_2$, the driving field assumes the form

$$\mathcal{E}(\mathbf{r},\tau) = E_1(\tau+t_1+t_2)\exp[i\mathbf{k}_1\mathbf{r}-i\bar{\omega}_1\tau+i\varphi_1(t_2,t_1)] + E_2(\tau+t_2)\exp[i\mathbf{k}_2\mathbf{r}-i\bar{\omega}_2\tau+i\varphi_2(t_2,t_1)] + E'(\tau+t')\exp[i\mathbf{k}'\mathbf{r}-i\bar{\omega}'\tau+i\varphi'(t_2,t_1)]+\text{c.c.}, \tag{C1}$$

where t' adopts the value of t_2 or t_2+t_1. t_1 and t_2 represent the time intervals in two-dimensional time-domain spectroscopy and φ_1, φ_2 represent the phase shifts between the pulses in a phase-locked measurement. The frequency domain $\bar{\mathcal{E}}(\omega)$ representation of the driving field adopts the form

$$\bar{\mathcal{E}}(\mathbf{r},\omega) = E_1(\omega-\bar{\omega}_1)\exp[i\mathbf{k}_1\mathbf{r}-i(\omega-\bar{\omega}_1)(t_1+t_2) + i\varphi_1(t_2,t_1)]+E_2(\omega-\bar{\omega}_2)\exp[i\mathbf{k}_2\mathbf{r}-i(\omega-\bar{\omega}_2) \times t_2+i\varphi_2(t_2,t_1)]+E'(\omega-\bar{\omega}')\exp[i\mathbf{k}'\mathbf{r}-i \times(\omega-\bar{\omega}')t'+i\varphi'(t_2,t_1)]+\text{c.c.}, \tag{C2}$$

where $E_1(\omega)$, $E_2(\omega)$, and $E'(\omega)$ are the Fourier transforms of the envelopes and E' is the pulse with which the system interacts twice ($E'=E_1'$ or $E'=E_2'$, depending on the technique).

We next introduce the heterodyne field, centered at $\tau=0$,

$$\mathcal{E}_h(\mathbf{r},\tau)=E_h(\tau)\exp(i\mathbf{k}_h\mathbf{r}-i\bar{\omega}_h\tau)+\text{c.c.} \tag{C3}$$

The polarization for the four techniques can be found by substituting Eq. (C2) into Eq. (B5) and keeping the contributions proportional to $E_2'E_2E_1^*$, $E_2^*E_1'E_1$, $E_2E_1'E_1^*$, and $E_2'E_2^*E_1$, respectively. The heterodyne signal is obtained upon the substitution of the expression for the polarization [Eq. (B5) together with Eq. (C2)] into Eq. (2.6). This yields the following expressions for the signals $S_j(t_2,t_1)$, $j=\text{I,II,III,IV}$ for the four techniques,

$$S_{\text{I}}(t_2,t_1)=\frac{1}{(2\pi)^3}\int d\omega_a\int d\omega_b\int d\omega_c\chi^{(3)}(-\omega_s;\omega_a,\omega_b,-\omega_c)\exp[-i(\omega_a+\omega_b)t_2+i\omega_c(t_1+t_2)] \times E_2'(\omega_a-\bar{\omega}_2')E_2(\omega_b-\bar{\omega}_2)E_1^*(\omega_c-\bar{\omega}_1)E_h^*(\omega_a+\omega_b-\omega_c-\bar{\omega}_h) \times\exp[-i[(\varphi_1(t_2,t_1)-\varphi_2'(t_2,t_1)-\varphi_2(t_2,t_1)+(\bar{\omega}_1-\bar{\omega}_2'-\bar{\omega}_2)t_2+\bar{\omega}_1t_1]], \tag{C4}$$

$$S_{\text{II}}(t_2,t_1)=\frac{1}{(2\pi)^3}\int d\omega_a\int d\omega_b\int d\omega_c\chi^{(3)}(-\omega_s;\omega_a,\omega_b,-\omega_c)\exp[-i(\omega_a+\omega_b)(t_1+t_2)+i\omega_ct_2] \times E_1'(\omega_a-\bar{\omega}_1')E_1(\omega_b-\bar{\omega}_1)E_2^*(\omega_c-\bar{\omega}_2)E_h^*(\omega_a+\omega_b-\omega_c-\bar{\omega}_h) \times\exp[-i[(\varphi_2(t_2,t_1)-\varphi_1'(t_2,t_1)-\varphi_1(t_2,t_1)-(\bar{\omega}_1'+\bar{\omega}_1)t_1+(\bar{\omega}_2-\bar{\omega}_1'-\bar{\omega}_1)t_2]], \tag{C5}$$

$$S_{\mathrm{III}}(t_2,t_1)=\frac{1}{(2\pi)^3}\int d\omega_a\int d\omega_b\int d\omega_c\chi^{(3)}(-\omega_s;\omega_a,\omega_b,-\omega_c)$$
$$\times\exp[-i(\omega_a+\omega_b)t_2+i\omega_c(t_1+t_2)-i\omega_a t_1]E_1'(\omega_a-\bar{\omega}_1')E_2(\omega_b-\bar{\omega}_2)$$
$$\times E_1^*(\omega_c-\bar{\omega}_1)E_h^*(\omega_a+\omega_b-\omega_c-\bar{\omega}_h)\exp[i[(\varphi_2(t_2,t_1)+\bar{\omega}_2 t_2]]. \tag{C6}$$

$$S_{\mathrm{IV}}(t_2,t_1)=\frac{1}{(2\pi)^3}\int d\omega_a\int d\omega_b\int d\omega_c\chi^{(3)}(-\omega_s;\omega_a,\omega_b,-\omega_c)$$
$$\times\exp[-i(\omega_a+\omega_b)t_2-i\omega_a t_1+i\omega_c t_2)]E_1(\omega_a-\bar{\omega}_1)E_2'(\omega_b-\bar{\omega}_2')$$
$$\times E_2^*(\omega_c-\bar{\omega}_2)E_h^*(\omega_a+\omega_b-\omega_c-\bar{\omega}_h)\exp[-i[-\varphi_1(t_2,t_1)-\bar{\omega}_1 t_1-\bar{\omega}_1 t_2]]. \tag{C7}$$

Equations (C4)–(C7) constitute the most general expressions for the heterodyne signal.

These expressions are simplified considerably in the impulsive limit, whereby all pulses are shorter than the inverse of the chromophore frequency differences and the linewidths. We set $\bar{\omega}_1=\bar{\omega}_2=\bar{\omega}_3=\bar{\omega}$, $E_1=E_2=E_3=E$ and assume that the detunings of $\bar{\omega}$ from the chromophore frequencies are small compared to the spectral width of the pulses. The envelopes in Eqs. (C4)–(C7) are broad in the frequency domain and can be set to a constant $\mathcal{F}$ which is given by the envelope area,

$$\mathcal{F}\equiv\int_{-\infty}^{\infty}d\tau E(\tau). \tag{C8}$$

The impulsive signals [Eqs. (C4)–(C7)] can then be represented in a form

$$S_j(t_2,t_1)$$
$$=|\mathcal{F}|^4\exp[if_j(t_2,t_1)]\frac{1}{(2\pi)^3}\int d\omega_a\int d\omega_b\int d\omega_c$$
$$\times\chi^{(3)}(-\omega_s;\omega_a,\omega_b,-\omega_c)$$
$$\times\exp[ig_j(t_2,t_1;\omega_a,\omega_b,\omega_c)], \tag{C9}$$

with

$$f_{\mathrm{I}}(t_2,t_1)\equiv\varphi_2'(t_2,t_1)+\varphi_2(t_2,t_1)-\varphi_1(t_2,t_1)-\bar{\omega}(t_1-t_2),$$
$$f_{\mathrm{II}}(t_2,t_1)\equiv\varphi_1'(t_2,t_1)+\varphi_1(t_2,t_1)-\varphi_2(t_2,t_1)+\bar{\omega}(2t_1+t_2),$$
$$f_{\mathrm{III}}(t_2,t_1)\equiv\varphi_2(t_2,t_1)+\bar{\omega}t_2, \tag{C10}$$
$$f_{\mathrm{IV}}(t_2,t_1)\equiv\varphi_1(t_2,t_1)+\bar{\omega}(t_1+t_2),$$

and

$$g_{\mathrm{I}}(t_2,t_1;\omega_a,\omega_b,\omega_c)\equiv-(\omega_a+\omega_b)t_2+\omega_c(t_1+t_2),$$
$$g_{\mathrm{II}}(t_2,t_1;\omega_a,\omega_b,\omega_c)\equiv-(\omega_a+\omega_b)(t_1+t_2)+\omega_c t_2,$$
$$g_{\mathrm{III}}(t_2,t_1;\omega_a,\omega_b,\omega_c)\equiv-(\omega_a+\omega_b)t_2+\omega_c(t_1+t_2)-\omega_a t_1,$$
$$g_{\mathrm{IV}}(t_2,t_1;\omega_a,\omega_b,\omega_c)\equiv-(\omega_a+\omega_b)t_2-\omega_a t_1+\omega_c t_2. \tag{C11}$$

Equations (C9)–(C11) give the impulsive signals in terms of the $\chi^{(3)}$. In Appendix D we combine them with Eq. (B8) to express the signal in terms of the one-exciton Green functions.

Our numerical calculations focused on structural information obtained from the coherent contribution only. Substituting Eq. (B8) into Eq. (C9) and noting that each of the permutations in Eq. (B8) gives the same result after integration, finally results in Eq. (2.10).

APPENDIX D: TIME-DOMAIN 2D SIGNALS IN THE EXCITON BASIS

In this appendix we express the heterodyne signal in terms of the one-exciton Green function, which has the following form in the frequency domain:

$$G_{mn}(\omega)=\sum_{\alpha}\frac{\varphi_\alpha(m)\varphi_\alpha^*(n)}{\omega-\epsilon_\alpha+i\Gamma}, \tag{D1}$$

where ϵ_α and $\varphi_\alpha(m)$ are the exciton energies and wavefunctions and Γ is the phenomenological width.

We start with Eq. (2.10) and assume $\mathcal{F}=1$ since the pulse envelope gives an overall factor in Eq. (2.10). We also chose the relative phases of the pulses in a way to get $f_j=0$. Substituting Eq. (D1) into Eq. (2.10) yields (for $j=1$)

$$S_{\mathrm{I}}(t_2,t_1)=\frac{1}{(2\pi)^3}\int d\omega\int d\omega_a\int d\omega_c\sum_{\alpha\beta\eta\nu}\mu_\alpha\mu_\beta\mu_\eta\mu_\nu$$
$$\times\exp[-i\omega t_2+i\omega_c(t_1+t_2)]\bar{\Gamma}_{\eta\nu,\alpha\beta}(\omega)$$
$$\times\frac{1}{\omega_a-\epsilon_\alpha+i\Gamma}\ \frac{1}{\omega-\omega_a-\epsilon_\beta+i\Gamma}$$
$$\times\frac{1}{\omega_c-\epsilon_\eta-i\Gamma}\ \frac{1}{\omega-\omega_c-\epsilon_\nu+i\Gamma}, \tag{D2}$$

where we have introduced the dipoles μ_α and the exciton scattering matrix in the exciton representation

$$\mu_\alpha \equiv \sum_m \mu_m \varphi_\alpha(m),$$
$$\overline{\Gamma}_{\eta\nu,\alpha\beta}(\omega) \equiv \sum_{mn} \varphi^*_\eta(m)\varphi^*_\nu(m)\varphi_\alpha(n)\varphi_\beta(n)\overline{\Gamma}_{mn}(\omega), \tag{D3}$$

Integrating over ω_1 and ω_3 yields

$$S_{\rm I}(t_2,t_1) = \frac{1}{2\pi}\exp[-\Gamma(t_1+t_2)]\sum_{\alpha\beta\eta\nu}\mu_\alpha\mu_\beta\mu_\eta\mu_\nu \times \int d\omega \overline{\Gamma}_{\eta\nu,\alpha\beta}(\omega)\frac{1}{\omega-(\epsilon_\alpha+\epsilon_\beta)+2i\Gamma} \times \frac{1}{\omega-(\epsilon_\eta+\epsilon_\nu)+i\gamma}\ [\exp[i\epsilon_\eta(t_1+t_2)-i\omega t_2] - \exp[-i\epsilon_\nu(t_1+t_2)+i\omega t_1]]. \tag{D4}$$

The expression in the r.h.s. of Eq. (D4) is regular at $\omega=\epsilon_\eta+\epsilon_\nu$ since the expression in the brackets vanishes at $\omega=\epsilon_\eta+\epsilon_\nu$; this allows to add $i\gamma$ to the resonant factor $[\omega-(\epsilon_\eta+\epsilon_\nu)]^{-1}$ and set it to $\gamma\to 0$. The sign of γ makes no difference and can be chosen for convenience. Taking $\gamma>0$, then only the first term in the brackets contributes to the integral. Since the poles of $\overline{\Gamma}(\omega)$ lie at $\mathrm{Im}(\omega)\approx -2i\Gamma$ it is convenient to deform the contour of integration to the lower half-plane with $\mathrm{Im}(\omega)=-\gamma_0$ for $\gamma_0\approx\Gamma$, which is accompanied by adding the contribution from the pole $\omega=\epsilon_\eta+\epsilon_\nu-i\gamma$ for $\gamma\to 0$. This yields $S_{\rm I}(t_2,t_1)$ in the form of two contributions. The other three techniques can be similarly calculated. We then have

$$S_j(t_2,t_1) = S_j^{(1)}(t_2,t_1) + S_j^{(2)}(t_2,t_1), \tag{D5}$$

with $j=$I,II,III,IV. We finally have

$$S_{\rm I}^{(1)}(t_2,t_1) = -\frac{i}{2}\exp[-\Gamma(t_1+t_2)]\sum_{\alpha\beta\eta\nu}\mu_\alpha\mu_\beta\mu_\eta\mu_\nu \times \frac{\overline{\Gamma}_{\eta\nu,\alpha\beta}(\epsilon_\eta+\epsilon_\nu)}{\epsilon_\eta+\epsilon_\nu-(\epsilon_\alpha+\epsilon_\beta)+2i\Gamma}\exp[i(\epsilon_\eta t_1-\epsilon_\nu t_2)], \tag{D6}$$

$$S_{\rm I}^{(2)}(t_2,t_1) = \frac{1}{2\pi}\exp[-\Gamma(t_1+t_2)-\gamma_0 t_2] \times \sum_{\alpha\beta\eta\nu}\mu_\alpha\mu_\beta\mu_\eta\mu_\nu\exp[i\epsilon_\eta(t_1+t_2)] \times \int d\omega \exp(-i\omega t_2)\overline{\Gamma}_{\eta\nu,\alpha\beta}(\omega-i\gamma_0) \times \frac{1}{\omega-(\epsilon_\alpha+\epsilon_\beta)+i(2\Gamma-\gamma_0)}\frac{1}{\omega-(\epsilon_\eta+\epsilon_\nu)-i\gamma_0}, \tag{D7}$$

$$S_{\rm II}^{(1)}(t_2,t_1) = -\frac{1}{2\pi}\exp(-\Gamma t_2-\gamma_0 t_1)\sum_{\alpha\beta\eta\nu}\mu_\alpha\mu_\beta\mu_\eta\mu_\nu \times \exp(-i\epsilon_\nu t_2)\int d\omega \exp(-i\omega t_1)\overline{\Gamma}_{\eta\nu,\alpha\beta}(\omega-i\gamma_0) \times \frac{1}{\omega-(\epsilon_\alpha+\epsilon_\beta)+i(2\Gamma-\gamma_0)}\frac{1}{\omega-(\epsilon_\eta+\epsilon_\nu)-i\gamma_0}, \tag{D8}$$

$$S_{\rm II}^{(2)}(t_2,t_1) = \frac{1}{2\pi}\exp[-\Gamma t_2-\gamma_0(t_1+t_2)]\sum_{\alpha\beta\eta\nu}\mu_\alpha\mu_\beta\mu_\eta\mu_\nu \times \exp(i\epsilon_\eta t_2)\int d\omega \exp[-i\omega(t_1+t_2)] \times \overline{\Gamma}_{\eta\nu,\alpha\beta}(\omega-i\gamma_0) \times \frac{1}{\omega-(\epsilon_\alpha+\epsilon_\beta)+i(2\Gamma-\gamma_0)}\frac{1}{\omega-(\epsilon_\eta+\epsilon_\nu)-i\gamma_0}, \tag{D9}$$

$$S_{\rm III}^{(1)}(t_2,t_1) = -\frac{i}{2}\exp[-\Gamma(t_2+2t_1)]\sum_{\alpha\beta\eta\nu}\mu_\alpha\mu_\beta\mu_\eta\mu_\nu \times \frac{\overline{\Gamma}_{\eta\nu,\alpha\beta}(\epsilon_\eta+\epsilon_\nu)}{\epsilon_\eta+\epsilon_\nu-(\epsilon_\alpha+\epsilon_\beta)+2i\Gamma} \times \exp[i(\epsilon_\eta-\epsilon_\alpha)t_1-i\epsilon_\nu t_2], \tag{D10}$$

$$S_{\rm III}^{(2)}(t_2,t_1) = \frac{1}{2\pi}\exp[-\Gamma(t_2+2t_1)-\gamma_0 t_2] \times \sum_{\alpha\beta\eta\nu}\mu_\alpha\mu_\beta\mu_\eta\mu_\nu\exp[i\epsilon_\eta t_2+i(\epsilon_\eta-\epsilon_\alpha)t_1] \times \int d\omega \exp(-i\omega t_2)\overline{\Gamma}_{\eta\nu,\alpha\beta}(\omega-i\gamma_0) \times \frac{1}{\omega-(\epsilon_\alpha+\epsilon_\beta)+i(2\Gamma-\gamma_0)}\frac{1}{\omega-(\epsilon_\eta+\epsilon_\nu)-i\gamma_0}, \tag{D11}$$

$$S_{\rm IV}^{(1)}(t_2,t_1) = -\frac{i}{2}\exp[-\Gamma(t_2+t_1)]\sum_{\alpha\beta\eta\nu}\mu_\alpha\mu_\beta\mu_\eta\mu_\nu \times \frac{\overline{\Gamma}_{\eta\nu,\alpha\beta}(\epsilon_\eta+\epsilon_\nu)}{\epsilon_\eta+\epsilon_\nu-(\epsilon_\alpha+\epsilon_\beta)+2i\Gamma}\exp(-i\epsilon_\alpha t_1-i\epsilon_\nu t_2), \tag{D12}$$

$$S_{\mathrm{IV}}^{(2)}(t_2,t_1)$$
$$=\frac{1}{2\pi}\exp[-\Gamma(t_2+t_1)-\gamma_0 t_2]\sum_{\alpha\beta\eta\nu}\mu_\alpha\mu_\beta\mu_\eta\mu_\nu$$
$$\times\exp(i\epsilon_\eta t_2-i\epsilon_\alpha t_1)\int d\omega$$
$$\times\exp(-i\omega t_2)\bar{\Gamma}_{\eta\nu,\alpha\beta}(\omega-i\gamma_0)$$
$$\times\frac{1}{\omega-(\epsilon_\alpha+\epsilon_\beta)+i(2\Gamma-\gamma_0)}\,\frac{1}{\omega-(\epsilon_\eta+\epsilon_\nu)-i\gamma_0}. \tag{D13}$$

The signals given by Eqs. (D5)–(D13) can be also expressed in terms of the contributions $R_{cj}(t_3,t_2,t_1)$ [Eqs. (A6)–(A8)] as outlined in Sec. II. We reiterate that such simple relations are not obvious from the very beginning and hold for a special choice of the relative phases of the pulses which yield $f_j=0$.

APPENDIX E: FINAL EXPRESSIONS FOR 2D SIGNALS

In this Appendix we carry out the Fourier transforms [Eq. (2.9)] to recast the results of Appendix B in the frequency domain. For techniques I (PE) we perform a double Fourier transform of Eqs. (D6) and (D7), this gives

$$S_{\mathrm{I}}^{(1)}(\Omega_2,\Omega_1)=\frac{i}{2}\sum_{\alpha\beta\eta\nu}\mu_\alpha\mu_\beta\mu_\eta\mu_\nu\,\frac{1}{\Omega_2-\epsilon_\nu+i\Gamma}$$
$$\times\frac{1}{\Omega_1+\epsilon_\eta+i\Gamma}\,\frac{\bar{\Gamma}_{\eta\nu,\alpha\beta}(\epsilon_\eta+\epsilon_\nu)}{\epsilon_\eta+\epsilon_\nu-(\epsilon_\alpha+\epsilon_\beta)+2i\Gamma}, \tag{E1}$$

$$S_{\mathrm{I}}^{(2)}(\Omega_2,\Omega_1)$$
$$=\frac{1}{2\pi}\sum_{\alpha\beta\eta\nu}\mu_\alpha\mu_\beta\mu_\eta\mu_\nu\,\frac{1}{\Omega_1+\epsilon_\eta+i\Gamma}$$
$$\times\int d\omega\bar{\Gamma}_{\eta\nu,\alpha\beta}(\omega-i\gamma_0)\,\frac{1}{\omega-\Omega_2-\epsilon_\eta-i(\Gamma+\gamma_0)}$$
$$\times\frac{1}{\omega-(\epsilon_\alpha+\epsilon_\beta)+i(2\Gamma-\gamma_0)}\,\frac{1}{\omega-(\epsilon_\eta+\epsilon_\nu)-i\gamma_0}. \tag{E2}$$

The reverse photon echo technique is obtained by a double Fourier transform of Eqs. (D8) and (D9),

$$S_{\mathrm{II}}^{(1)}(\Omega_2,\Omega_1)$$
$$=-\frac{1}{2\pi}\sum_{\alpha\beta\eta\nu}\mu_\alpha\mu_\beta\mu_\eta\mu_\nu\,\frac{1}{\Omega_2-\epsilon_\nu+i\Gamma}$$
$$\times\int d\omega\bar{\Gamma}_{\eta\nu,\alpha\beta}(\omega-i\gamma_0)\,\frac{1}{\omega-\Omega_1-i\gamma_0}$$
$$\times\frac{1}{\omega-(\epsilon_\alpha+\epsilon_\beta)+i(2\Gamma-\gamma_0)}\,\frac{1}{\omega-(\epsilon_\eta+\epsilon_\nu)-i\gamma_0}, \tag{E3}$$

$$S_{\mathrm{II}}^{(2)}(\Omega_2,\Omega_1)$$
$$=-\frac{1}{2\pi}\sum_{\alpha\beta\eta\nu}\mu_\alpha\mu_\beta\mu_\eta\mu_\nu\int d\omega\bar{\Gamma}_{\eta\nu,\alpha\beta}(\omega-i\gamma_0)$$
$$\times\frac{1}{\omega-\Omega_1-i\gamma_0}\,\frac{1}{\omega-\Omega_2-\epsilon_\eta-i(\Gamma+\gamma_0)}$$
$$\times\frac{1}{\omega-(\epsilon_\alpha+\epsilon_\beta)+i(2\Gamma-\gamma_0)}\,\frac{1}{\omega-(\epsilon_\eta+\epsilon_\nu)-i\gamma_0}. \tag{E4}$$

The third technique (TG) is obtained from Eqs. (D10) and (D11),

$$S_{\mathrm{III}}^{(1)}(\Omega_2,\Omega_1)$$
$$=\frac{i}{2}\sum_{\alpha\beta\eta\nu}\mu_\alpha\mu_\beta\mu_\eta\mu_\nu\,\frac{1}{\Omega_2-\epsilon_\nu+i\Gamma}\,\frac{1}{\Omega_1+\epsilon_\eta-\epsilon_\alpha+2i\Gamma}$$
$$\times\frac{\bar{\Gamma}_{\eta\nu,\alpha\beta}(\epsilon_\eta+\epsilon_\nu)}{\epsilon_\eta+\epsilon_\nu-(\epsilon_\alpha+\epsilon_\beta)+2i\Gamma}, \tag{E5}$$

$$S_{\mathrm{III}}^{(2)}(\Omega_2,\Omega_1)$$
$$=\frac{1}{2\pi}\sum_{\alpha\beta\eta\nu}\mu_\alpha\mu_\beta\mu_\eta\mu_\nu\,\frac{1}{\Omega_1+\epsilon_\eta-\epsilon_\alpha+2i\Gamma}$$
$$\times\int d\omega\bar{\Gamma}_{\eta\nu,\alpha\beta}(\omega-i\gamma_0)\,\frac{1}{\omega-\Omega_2-\epsilon_\eta-i(\Gamma+\gamma_0)}$$
$$\times\frac{1}{\omega-(\epsilon_\alpha+\epsilon_\beta)+i(2\Gamma-\gamma_0)}\,\frac{1}{\omega-(\epsilon_\eta+\epsilon_\nu)-i\gamma_0}. \tag{E6}$$

Finally, the fourth technique (RTG) is obtained from Eqs. (D12) and (D13),

$$S_{\mathrm{IV}}^{(1)}(\Omega_2,\Omega_1)=\frac{i}{2}\sum_{\alpha\beta\eta\nu}\mu_\alpha\mu_\beta\mu_\eta\mu_\nu\,\frac{1}{\Omega_2-\epsilon_\nu+i\Gamma}$$
$$\times\frac{1}{\Omega_1-\epsilon_\alpha+i\Gamma}\,\frac{\bar{\Gamma}_{\eta\nu,\alpha\beta}(\epsilon_\eta+\epsilon_\nu)}{\epsilon_\eta+\epsilon_\nu-(\epsilon_\alpha+\epsilon_\beta)+2i\Gamma}, \tag{E7}$$

$$S_{\mathrm{IV}}^{(2)}(\Omega_2,\Omega_1)$$
$$=\frac{1}{2\pi}\sum_{\alpha\beta\eta\nu}\mu_\alpha\mu_\beta\mu_\eta\mu_\nu\,\frac{1}{\Omega_1-\epsilon_\alpha+i\Gamma}$$
$$\times\int d\omega\bar{\Gamma}_{\eta\nu,\alpha\beta}(\omega-i\gamma_0)\,\frac{1}{\omega-\Omega_2-\epsilon_\eta-i(\Gamma+\gamma_0)}$$
$$\times\frac{1}{\omega-(\epsilon_\alpha+\epsilon_\beta)+i(2\Gamma-\gamma_0)}\,\frac{1}{\omega-(\epsilon_\eta+\epsilon_\nu)-i\gamma_0}. \tag{E8}$$

APPENDIX F: PERTURBATIVE EXPANSION OF 2D SIGNALS IN EXCITONIC COUPLINGS

When the intermolecular coupling constants are small compared with the dephasing rates, the optical susceptibility

can be expanded in powers of J, retaining only the zero- and first-order terms; the former describe the response of uncoupled chromophores, whereas the latter represent the coupling-induced peaks. The perturbative calculations were carried out for a slightly more general form of the dephasing matrix, where each chromophore has its own dephasing rate $\Gamma_{mn}=\Gamma_n\delta_{mn}$ (throughout this paper we assumed $\Gamma_n=\Gamma$, independent on n). The desired expansion can be obtained by expanding the Green functions $G_{mn}(\omega)$ in the GFE for $R^{(3)}$ [Eq. (B8)] (we recall that $\overline{\Gamma}_{mn}(\omega)$ is expressed in terms of one-exciton Green function and does not have first-order corrections in J),

$$G_{mn}(\omega)=\frac{1}{\omega-\Omega_m+i\Gamma_m}\,\delta_{mn}+\frac{1}{\omega-\Omega_m+i\Gamma_m}\,J_{mn}\,\frac{1}{\omega-\Omega_n+i\Gamma_n}. \tag{F1}$$

Introducing the $R_n^{(3)}$ of a single chromophore

$$R_n^{(3)}\equiv\frac{\omega_1+\omega_2-2\Omega_n+2i\Gamma_n}{(\omega_1-\Omega_n+i\Gamma_n)(\omega_2-\Omega_n+i\Gamma_n)(\omega_3-\Omega_n-i\Gamma_n)(\omega_s-\Omega_n+i\Gamma_n)}, \tag{F2}$$

Eq. (B8) then adopts the form

$$\begin{aligned}R^{(3)}(-\omega_s;\omega_1,\omega_2,-\omega_3)&=\sum_n(\mu_n)^4R_n^{(3)}(-\omega_s;\omega_1,\omega_2,-\omega_3)\\&+\sum_{mn}J_{mn}\mu_m(\mu_n)^3R_n^{(3)}(-\omega_s;\omega_1,\omega_2,-\omega_3)\\&\times\left[\frac{1}{\omega_1-\Omega_m+i\Gamma_m}+\frac{1}{\omega_2-\Omega_m+i\Gamma_m}+\frac{1}{\omega_s-\Omega_m+i\Gamma_m}+\frac{1}{\omega_3-\Omega_m-i\Gamma_m}\right].\end{aligned} \tag{F3}$$

The impulsive signal for the weak coupling case can be obtained by substituting Eq. (F3) into Eq. (C9) and can be represented in the form

$$S_j(t_2,t_1)=S_j^{(\mathrm{TL})}(t_2,t_1)+\Delta S_j(t_2,t_1)+S_j^{(\mathrm{CP})}(t_2,t_1), \tag{F4}$$

where $S_j^{(TL)}$ represents the signal from uncoupled two-level molecules, $\Delta S_j(t_2,t_1)$ represents an intermolecular coupling induced correction to $S_j^{(\mathrm{TL})}$, whereas $S_j^{(\mathrm{CP})}(t_2,t_1)$ represents the cross peaks which originate from intermolecular coupling ($j=$I,II,III,IV). A straightforward calculation yields (assuming factor $\mathcal{F}=1$ and phases $f_j=0$)

$$S_{\mathrm{I}}^{(\mathrm{TL})}(t_2,t_1)=\sum_n(\mu_n)^4\exp[i\epsilon_n(t_1-t_2)-\Gamma_n(t_1+t_2)], \tag{F5}$$

$$\begin{aligned}\Delta S_{\mathrm{I}}(t_2,t_1)&=\sum_{mn}^{m\neq n}J_{mn}\mu_m(\mu_n)^3\exp[i\epsilon_n(t_1-t_2)-\Gamma_n(t_1+t_2)]\\&\times\left[\frac{2}{\epsilon_n-\epsilon_m+i(\Gamma_m+\Gamma_n)}+\frac{2(\epsilon_n-\epsilon_m)}{(\epsilon_n-\epsilon_m)^2+(\Gamma_m+\Gamma_n)^2}\right],\end{aligned} \tag{F6}$$

$$\begin{aligned}S_{\mathrm{I}}^{(\mathrm{CP})}(t_2,t_1)=\sum_{mn}^{m\neq n}J_{mn}\mu_m(\mu_n)^3\Bigg\{&\exp[i(\epsilon_nt_1-\epsilon_mt_2)]\\&\times\left[\frac{2\exp[-\Gamma_nt_1-(2\Gamma_n+\Gamma_m)t_2]}{\epsilon_m-\epsilon_n}+\frac{\exp[-\Gamma_nt_1-\Gamma_mt_2]}{\epsilon_m-\epsilon_n+i(\Gamma_n-\Gamma_m)}\right]\\&+\frac{\exp[i(\epsilon_mt_1-\epsilon_nt_2)-\Gamma_mt_1-\Gamma_nt_2]}{\epsilon_m-\epsilon_n+i(\Gamma_m-\Gamma_n)}\Bigg\},\end{aligned} \tag{F7}$$

$$S_{\mathrm{II}}^{(\mathrm{TL})}(t_2,t_1)=0, \tag{F8}$$

$$\Delta S_{\mathrm{II}}(t_2,t_1)=0, \tag{F9}$$

$$\begin{aligned}S_{\mathrm{II}}^{(\mathrm{CP})}(t_2,t_1)=\sum_{mn}^{m\neq n}J_{mn}\mu_m(\mu_n)^3\frac{2}{\epsilon_m-\epsilon_n-i(\Gamma_m+\Gamma_n)}&\\\times[\exp[-i(\epsilon_m+\epsilon_n)t_1-(\Gamma_m+\Gamma_n)t_1]\exp[-i\epsilon_mt_2-(\Gamma_m+2\Gamma_n)t_2]&\\-\exp[-i(\epsilon_m+\epsilon_n)t_1-(\Gamma_m+\Gamma_n)t_1]\exp[-i\epsilon_nt_2-\Gamma_nt_2]],&\end{aligned} \tag{F10}$$

$$S_{\mathrm{III}}^{(\mathrm{TL})}(t_2,t_1)=\sum_n(\mu_n)^4\exp[-i\epsilon_nt_2-\Gamma_n(t_1+t_2)], \tag{F11}$$

$$\Delta S_{\mathrm{III}}(t_2,t_1)=\sum_{mn}^{m\neq n} J_{mn}\mu_m(\mu_n)^3\exp[-2\Gamma_n t_1-i(\epsilon_n-i\Gamma_n)t_2]\left[\frac{2}{\epsilon_n-\epsilon_m+i(\Gamma_m-\Gamma_n)}\right.$$
$$\left.+\frac{1}{\epsilon_n-\epsilon_m+i(\Gamma_m+\Gamma_n)}+\frac{1}{\epsilon_n-\epsilon_m+i(\Gamma_n-\Gamma_m)}\right], \tag{F12}$$

$$S_{\mathrm{III}}^{(\mathrm{CP})}(t_2,t_1)=\sum_{mn}^{m\neq n} J_{mn}\mu_m(\mu_n)^3\left[\frac{\exp\{-i[\epsilon_m-\epsilon_n-i(\Gamma_m+\Gamma_n)]t_1-i(\epsilon_n-i\Gamma_n)t_2\}}{\epsilon_m-\epsilon_n+i(\Gamma_n-\Gamma_m)}\right.$$
$$+\frac{1}{\epsilon_n-\epsilon_m+i(\Gamma_m+\Gamma_n)}\exp\{-i[\epsilon_m-\epsilon_n-i(\Gamma_m+\Gamma_n)]t_1-i(\epsilon_n-i\Gamma_n)t_2\}$$
$$+\frac{1}{\epsilon_m-\epsilon_n+i(\Gamma_m-\Gamma_n)}\exp\{-i[\epsilon_n-\epsilon_m-i(\Gamma_m+\Gamma_n)]t_1-i(\epsilon_n-i\Gamma_n)t_2\}$$
$$\left.+\frac{1}{\epsilon_m-\epsilon_n+i(\Gamma_n-\Gamma_m)}\exp[-2\Gamma_n t_1-i(\epsilon_m-i\Gamma_m)t_2]\right], \tag{F13}$$

$$S_{\mathrm{IV}}^{(\mathrm{TL})}(t_2,t_1)=\sum_n (\mu_n)^4\exp[-i\epsilon_n(t_1+t_2)-\Gamma_n(t_1+t_2)], \tag{F14}$$

$$\Delta S_{\mathrm{IV}}(t_2,t_1)=\sum_{mn}^{m\neq n} J_{mn}\mu_m(\mu_n)^3\frac{\exp[-i(\epsilon_n-i\Gamma_n)(t_1+t_2)]}{(\epsilon_n-\epsilon_m)+i(\Gamma_m+\Gamma_n)}, \tag{F15}$$

$$S_{\mathrm{IV}}^{(\mathrm{CP})}(t_2,t_1)=\sum_{mn}^{m\neq n} J_{mn}\mu_m(\mu_n)^3\frac{\exp[-i(\epsilon_m-i\Gamma_m)t_1-i(\epsilon_n-i\Gamma_n)t_2)]}{\epsilon_n-\epsilon_m+i(\Gamma_m+\Gamma_n)}. \tag{F16}$$

[1] R. R. Ernst, G. Bodenhausen, and A. Wokaun, *Principles of Nuclear Magnetic Resonance in One and Two Dimensions* (Clarendon Press, Oxford, 1987); J. K. M. Sanders and B. K. Hunter, *Modern NMR Spectroscopy* (Oxford, New York, 1993).
[2] J. N. Evans, *Biomolecular NMR Spectroscopy* (Oxford, New York, 1995).
[3] *Ultrafast Phenomena XI*, edited by T. Elsasser, J. G. Fujimoto, D. Wiersma, and W. Zinth (Springer, Berlin, 1998).
[4] A. W. Weiner, D. E. Leird, G. P. Weiderrecht, and K. A. Nelson, Science **247**, 1317 (1990).
[5] J. X. Tull, M. A. Dugan, and W. S. Warren, Adv. Magn. Opt. Reson. **20**, 1 (1997).
[6] W. P. de Boeij, M. S. Pshenichnikov, and D. A. Wiersma, Chem. Phys. Lett. **238**, 1 (1995); **247**, 264 (1995).
[7] N. F. Scherer, A. J. Ruggiero, M. Du, and G. R. Fleming, J. Chem. Phys. **93**, 856 (1990).
[8] M. G. Cory, M. C. Zerner, X. Hu, and K. Schulten, J. Phys. Chem. B **102**, 7640 (1998).
[9] S. Mukamel, *Principles of Nonlinear Optical Spectroscopy* (Oxford, New York, 1995).
[10] Y. Tanimura and S. Mukamel, J. Chem. Phys. **99**, 9496 (1993).
[11] W. M. Zhang, V. Chernyak, and S. Mukamel, in *Ultrafast Phenomena XI*, edited by T. Elsasser, J. G. Fujimoto, D. A. Wiersma, and W. Zinth (Springer, Berlin, 1998), p. 663; S. Mukamel, W. M. Zhang, and V. Chernyak, in *Proceeding of the XIth International Congress on Photosynthesis*, edited by G. Garab and J. Pusztai (Kluwer Academic, The Netherlands, 1998).
[12] S. Mukamel, A. Piryatinski, and V. Chernyak, Acc. Chem. Phys. **32**, 145 (1999).
[13] *J-Aggregates*, edited by T. Kobayashi (World Scientific, Singapore, 1996).
[14] R. van Grondelle, J. P. Dekker, T. Gillbro, and V. Sundström, Biochim. Biophys. Acta **1187**, 1 (1994).
[15] V. Sundström and R. van Grondelle, in *Anoxygenic Photosynthetic Bacteria*, edited by R. E. Blankenship, M. T. Madiga, and C. E. Baner (Kluwer Academic, Dordrecht, 1995), p. 349.
[16] R. J. W. Louwe, J. Vrieze, A. J. Hoff, and T. J. Aartsma, J. Phys. Chem. B **101**, 11280 (1997).
[17] S. I. E. Vulto, M. A. de Baat, R. J. W. Louwe, H. P. Permentier, T. Neef, M. Miller, H. van Amerongen, and T. J. Aartsma (preprint).
[18] C. C. Gradinaru, S. Ozdemir, D. Gulen, I. H. M. van Stokkum, R. van Grondelle, and H. van Amerongen, Biophys. J. **75**, 3064 (1998).
[19] J. P. Connelly, M. G. Muller, M. Hucke, G. Gatzen, C. W. Mullineaux, A. V. Ruban, P. Horton, and A. R. Holzwarth, J. Phys. Chem. B **101**, 1902 (1997).
[20] C. C. Gradinaru, A. A. Pascal, F. van Mourik, B. Robert, P. Horton, R. van Grondelle, and H. van Amerongen, Biochemistry **37**, 1143 (1998).
[21] T. Pullerits, M. Chachisvilis, and V. Sundström, J. Phys. Chem. **100**, 10787 (1996).
[22] V. Nagarajan, R. G. Alden, J. C. Williams, and W. W. Parson, Proc. Natl. Acad. Sci. USA **93**, 13774 (1996).
[23] R. Jimenez, F. van Mourik, J. Y. Yu, and G. R. Fleming, J. Phys. Chem. B **101**, 7350 (1997).
[24] J. Y. Yu, Y. Nagasawa, R. van Grondelle, and G. R. Fleming, Chem. Phys. Lett. **280**, 404 (1997).
[25] T. Joo and A. C. Albrecht, Chem. Phys. **176**, 233 (1993).
[26] N. R. S. Reddy, R. J. Cogdell, L. Zhao, and G. J. Small, Photochem. Photobiol. **57**, 35 (1993).
[27] C. D. Caro, R. W. Visschers, R. van Grondelle, and S. Völker, J. Phys. Chem. **98**, 10584 (1994).
[28] X. Hu and K. Schulten, Physics Today **1997**, Aug., p. 28.
[29] A. J. Hoff and J. Deisenhofer, Phys. Rep. **287**, 1 (1997).
[30] T. Pullerits and V. Sundström, Acc. Chem. Res. **29**, 381 (1996).
[31] W. M. Zhang, T. Meier, V. Chernyak, and S. Mukamel, J. Chem. Phys. **108**, 7763 (1998); Philos. Trans. R. Soc. London, Ser. A **356**, 405 (1998).
[32] T. E. Creighton, *Proteins: Structures and Molecular Properties*, 2nd ed. (Freeman, New York, 1993).
[33] S. Krimm and J. Bandeker, Adv. Protein Chem. **38**, 181 (1986).
[34] E. A. Silinsh and V. Čápek, *Organic Molecular Crystals* (American Institute of Physics, New York, 1994).
[35] W. K. Surewicz, H. H. Mantch, and D. Chapman, Biochemistry **32**, 389 (1993).
[36] M. Leckson and H. Mantsch, Crit. Rev. Biochem. Mol. Biol. **30**, 95 (1995).

[37] H. Torii and M. Tasumi, J. Chem. Phys. **96**, 3379 (1992).
[38] P. Hamm, M. Lim, and R. M. Hochstrasser, J. Phys. Chem. B **102**, 6123 (1998).
[39] A. Tokmakoff, M. J. Lang, D. S. Larson, G. R. Fleming, V. Chernyak, and S. Mukamel, Phys. Rev. Lett. **79**, 2702 (1997).
[40] S. Mukamel and D. S. Chemla, Chem. Phys. **210** (1996) (special issue).
[41] J. C. Deàk, L. K. Iwaki, and D. D. Dlott, J. Phys. Chem. A **102**, 8193 (1998); Chem. Phys. Lett. **293**, 405 (1998).
[42] V. Chernyak, W. M. Zhang, and S. Mukamel, J. Chem. Phys. **109**, 9587 (1998).
[43] F. C. Spano and S. Mukamel, Phys. Rev. A **40**, 5783 (1989); Phys. Rev. Lett. **66**, 1197 (1991); J. Chem. Phys. **95**, 7526 (1991).
[44] J. A. Leegwater and S. Mukamel, Phys. Rev. A **46**, 452 (1992).
[45] V. Chernyak, N. Wang, and S. Mukamel, Phys. Rep. **263**, 213 (1995).
[46] O. Kühn, V. Chernyak, and S. Mukamel, J. Chem. Phys. **105**, 8586 (1996).
[47] T. Meier, V. Chernyak, and S. Mukamel, J. Phys. Chem. B **101**, 7332 (1997).
[48] R. Zwanzig, Lect. Theor. Phys. **3**, 106 (1961); Physica (Amsterdam) **30**, 1109 (1964).
[49] N. Bloembergen, *Nonlinear Optics* (Benjamin, New York, 1965).
[50] M. Cho, N. F. Scherer, G. R. Fleming, and S. Mukamel, J. Chem. Phys. **96**, 5618 (1992).
[51] P. Vöhringer and N. F. Scherer, J. Phys. Chem. **99**, 2684 (1995).
[52] J. A. Leegwater and S. Mukamel, J. Chem. Phys. **101**, 7388 (1994).
[53] S. Schmitt-Rink, S. Mukamel, K. Leo, J. Shah, and D. S. Chemla, Phys. Rev. A **44**, 2124 (1991).
[54] J. Seth, V. Palaniappan, R. W. Wagner, T. E. Johnson, J. S. Lindsey, and D. F. Bocian, J. Am. Chem. Soc. **118**, 11194 (1996); D. L. Jiang and T. Aida, J. Am. Chem. Soc. **120**, 10895 (1998); T. Aida (private communication).
[55] (a) M. R. Wasielewski in *Chlorophylls*, edited by H. Scheer (Chemical Rubber, Boca Raton, 1991), pp. 269–286; (b) Chem. Rev. **92**, 435 (1992).
[56] In the perturbative expansion given in Appendix E we assume a slightly more general form, where the dephasing rate depends on the site $\Gamma_{mn} = \Gamma_n \delta_{mn}$.
[57] V. Chernyak and S. Mukamel, J. Opt. Soc. Am. B **13**, 1302 (1996).
[58] A. G. Redfield, Adv. Magn. Reson. **1**, 1 (1965).
[59] W. T. Pollard, A. K. Felts, and R. A. Friesner, Adv. Chem. Phys. **93**, 77 (1996).
[60] S. Mukamel and R. F. Loring, J. Opt. Soc. Am. B **3**, 595 (1986).
[61] V. Chernyak and S. Mukamel, Phys. Rev. B **48**, 2470 (1993).